ENERGY DENSITY GRADIENT ESTIMATION FOR MONTE CARLO METHODS IN MIX MODELS

A Thesis

by

TAYLOR KINSEY LANE

Submitted to the Office of Graduate and Professional Studies of
Texas A&M University
in partial fulfillment of the requirements for the degree of

MASTER OF SCIENCE

Chair of Committee,	Ryan G. McClarren
Committee Members,	Diego A. Donzis
	Pavel V. Tsvetkov
Head of Department,	Yassin A. Hassan

December 2015

Major Subject: Nuclear Engineering

ABSTRACT

A common method to solving coupled radiation-hydrodynamics simulations is to use the Implicit Monte Carlo method as the radiation solve and the BHR-2 mix model for the hydrodynamics solve. This methodology has been shown to be susceptible to the stochastic noise inherent to IMC. This thesis shows why the BHR-2 is susceptible to the noise, and why linear filters are not the best solution to alleviating this susceptibility. A finite element representation is derived to approximate the gradient of the energy density, which is the coupling quantity between the radiation and hydrodynamics solve. Results using this finite element estimator, are presented for two problems of different complexity, and compared to results using a finite difference method to approximate the energy density gradient. The estimator is shown to reduce the variance in the gradient, which would lead to a decrease in the computational cost of IMC/BHR-2 simulations, and increase their robustness to stochastic noise.

ACKNOWLEDGEMENTS

The author would like to acknowledge the guidance and direction of Todd Urbatsch. His feedback during the defense and editing process was extremely valuable.

NOMENCLATURE

BHR	Besnard-Harlow-Rauenzahn
FINMCOOL	Fully Implicit Monte Carlo Object-Oriented Language (IMC code developed at TAMU)
IMC	Implicit Monte Carlo
jk	jerk (unit of energy equivalent to 10^9 Joules)
KH	Kelvin-Helmholtz
LANL	Los Alamos National Laboratory
LTE	Local Thermodynamic Equilibrium
QoI	Quantity of Interest
RANS	Reynolds-Averaged Navier-Stokes equations
RM	Richtmyer-Meshkov
RT	Rayleigh-Taylor
sh	shake (unit of time equivalent to 10^{-8} seconds)
TAMU	Texas A&M University
TRT	Thermal Radiative Transfer

TABLE OF CONTENTS

Page

LIST OF FIGURES

FIGURE Page

LIST OF TABLES

TABLE Page

1. INTRODUCTION

The ever-expanding capabilities of modern supercomputing machines have led to a push for simulations to be able to simultaneously solve multiple physical phenomena, typically in completely differing physical regimes. These capabilities in these simulations, so-called *multi-physics codes*, are a driving force in the motivation for this thesis. A solution technique for a specific physical model may be accurate when the model is solved independently, however when the model is coupled in a multi-physics code, the code may yield inaccurate results caused by the solution technique. An example of such behavior is the coupling of a Reynolds-Averaged Navier-Stokes (RANS) hydrodynamics model, such as BHR2, to a stochastic radiation transport model such as Implicit Monte Carlo (IMC).

The ability to couple radiative transfer and hydrodynamics models has a wide range of applications: inertial confinement fusion, astrophysical processes, and stockpile stewardship, to name a few. All of these applications hinge on the multi-physics simulation's ability to accurately treat the material boundary and the amount of material mixing caused by turbulent processes.

This work shows why a manageable drawback to the IMC method, stochastic noise in the energy density, is exacerbated when coupled to the BHR2 model via the pressure gradient. Furthermore, it shows how the gradient of the net deposited energy density can computed without a finite difference over noisy data using FINMCOOL, an IMC code developed at Texas A&M University. This, in turn, leads to a smoother pressure gradient term for the BHR2 model which leads to less noise-seeded Rayleigh-Taylor instabilities at the material interface.

1.1 The BHR2 Model

The BHR model [2], a turbulence model for variable density and compressible flows developed at Los Alamos National Laboratory, is closed set of equations that evolve the quantities needed to close the Reynolds-averaged Navier-Stokes (RANS) equations. BHR2 aims to model the physics involved in variable density turbulence, including Kelvin-Helmholtz (KH) [5, 7], Rayleigh-Taylor (RT) [12, 16], and Richtmyer-Meshkov (RM) [13, 11] turbulence-driven instabilities. The original derivation of the governing equations and the assumptions used for closure of the BHR model can be found in Ref. [2], as well as some variations of the original model [15, 3, 8, 14, 1]. Therefore, the derivation of the BHR model will not be presented here. However, it is important to note that RANS equations can employ ensemble averaging using both Reynolds decomposition and Favre decomposition. An ensemble average is typically determined following many experiments or simulations which give a distribution of results consisting of a mean and a deviation (or fluctuation) from the mean. Reynolds decomposition is a uniformly-weighted average,

$$X = \bar{X} + X', \tag{1.1}$$

where X is a QoI, the overbar denotes the mean and the single prime denotes the fluctuating component. Similarly, Favre decomposition is a mass-weighted average,

$$X = \tilde{X} + X'', \tag{1.2}$$

where the tilde is the mass-weighted average component of the QoI X,

$$\tilde{X} = \frac{\overline{\rho X}}{\bar{\rho}}, \tag{1.3}$$

and the fluctuating component about $\tilde{X}$ is represented by the double prime. This notation is used throughout the thesis. The three-dimensional BHR2 equations, as implemented in RAGE, are given by,

$$\frac{\partial \bar{\rho} K}{\partial t} + \underbrace{\frac{\partial \bar{\rho} K \tilde{u}_n}{\partial x_n}}_{\text{Advection}} = \underbrace{a_n \frac{\partial \bar{P}}{\partial x_n}}_{\substack{\text{Buoyancy} \\ \text{Production}}} - \underbrace{R_{in} \frac{\partial \tilde{u}_n}{\partial x_n}}_{\substack{\text{Shear} \\ \text{Production}}} + \underbrace{\frac{\partial}{\partial x_n}\left(\frac{\bar{\rho}\nu_t}{\sigma_k}\frac{\partial K}{\partial x_n}\right)}_{\substack{\text{Turbulent Transport} \\ \text{(Diffusion)}}} - \underbrace{\bar{\rho}\frac{K^{3/2}}{L}}_{\substack{\text{Turbulent} \\ \text{Dissipation}}}, \tag{1.4a}$$

$$\begin{aligned}\frac{\partial \bar{\rho} L}{\partial t} + \underbrace{\frac{\partial \bar{\rho} L \tilde{u}_n}{\partial x_n}}_{\text{Advection}} = \frac{L}{K}\Bigg[& \underbrace{\left(\frac{3}{2} - C_4\right) a_n \frac{\partial \bar{P}}{\partial x_n}}_{\text{Buoyancy Production}} - \underbrace{\left(\frac{3}{2} - C_1\right) R_{in} \frac{\partial \tilde{u}_n}{\partial x_n}}_{\text{Shear Production}}\Bigg] \\ & - \underbrace{C_3 \bar{\rho} L \frac{\partial \tilde{u}_n}{\partial x_n}}_{\substack{\text{Shear} \\ \text{Production}}} + \underbrace{\frac{\partial}{\partial x_n}\left(\frac{\bar{\rho}\nu_t}{\sigma_\epsilon}\frac{\partial L}{\partial x_n}\right)}_{\substack{\text{Turbulent Transport} \\ \text{(Diffusion)}}} - \underbrace{\left(\frac{3}{2} - C_2\right)\bar{\rho} K^{1/2}}_{\substack{\text{Turbulent} \\ \text{Dissipation}}},\end{aligned} \tag{1.4b}$$

$$\begin{aligned}\frac{\partial \bar{\rho} a_i}{\partial t} + \underbrace{\frac{\partial \bar{\rho} a_i \tilde{u}_n}{\partial x_n}}_{\text{Advection}} = & \underbrace{C_{a2} b \frac{\partial \bar{P}}{\partial x_n}}_{\substack{\text{Buoyancy} \\ \text{Production}}} - \underbrace{\frac{R_{in}}{\rho}\frac{\partial \bar{\rho}}{\partial x_n}}_{\substack{\text{Production}}} - \underbrace{\bar{\rho} a_n \frac{\partial(\tilde{u}_i - a_i)}{\partial x_n}}_{\text{Production}} + \underbrace{\bar{\rho}\frac{\partial a_i a_n}{\partial x_n}}_{\substack{\text{Transport}}} \\ & + \underbrace{\frac{\partial}{\partial x_n}\left(\frac{\nu_t}{\bar{\rho}\sigma_a}\frac{\partial a_i}{\partial x_n}\right)}_{\substack{\text{Turbulent Transport} \\ \text{(Diffusion)}}} - \underbrace{C_{a1}\bar{\rho} a_i \frac{K^{1/2}}{L}}_{\substack{\text{Turbulent} \\ \text{Dissipation}}},\end{aligned} \tag{1.4c}$$

$$\frac{\partial \bar{\rho} b}{\partial t} + \underbrace{\frac{\partial \bar{\rho} b \tilde{u}_n}{\partial x_n}}_{\text{Advection}} = \underbrace{2\bar{\rho} a_n \frac{\partial b}{\partial x_n}}_{\text{Production}} - \underbrace{2\left(b+1\right) a_n \frac{\partial \bar{\rho}}{\partial x_n}}_{\text{Production}} + \underbrace{\bar{\rho}^2 \frac{\partial}{\partial x_n}\left(\frac{\nu_t}{\bar{\rho}\sigma_b}\frac{\partial b}{\partial x_n}\right)}_{\substack{\text{Turbulent Transport} \\ \text{(Diffusion)}}} - \underbrace{C_b \bar{\rho}\frac{K^{1/2}}{L} b}_{\substack{\text{Turbulent} \\ \text{Dissipation}}}, \tag{1.4d}$$

and

$$\frac{\partial \bar{\rho} \tilde{c^k}}{\partial t} + \underbrace{\frac{\partial \bar{\rho} \tilde{c^k} \tilde{u}_n}{\partial x_n}}_{\text{Advection}} = \underbrace{\frac{\partial}{\partial x_n}\left(\frac{\bar{\rho}\nu_t}{\sigma_c}\frac{\partial \tilde{c^k}}{\partial x_n}\right)}_{\text{Diffusion}}, \tag{1.4e}$$

where

$$R = \text{Reynolds stress tensor}, \tag{1.5a}$$

$$K = \frac{1}{2}\text{tr}\,(R) = \text{turbulent kinetic energy}, \tag{1.5b}$$

$$L = \text{turbulent length scale}, \tag{1.5c}$$

$$a = \text{turbulent mass flux velocity}, \tag{1.5d}$$

$$b = -\overline{\rho' \left(\frac{1}{\rho}\right)'} = \text{density-specific volume correlation}, \tag{1.5e}$$

$$x = \text{position vector}, \tag{1.5f}$$

$$t = \text{time}, \tag{1.5g}$$

$$\bar{\rho} = \text{uniformly-weighted average fluid density}, \tag{1.5h}$$

$$\bar{P} = \text{uniformly-weighted average pressure}, \tag{1.5i}$$

$$\tilde{u} = \text{mass-weighted average fluid velocity}, \tag{1.5j}$$

$$\nu_t = C_\mu L\sqrt{K} = \text{turbulent viscosity}, \tag{1.5k}$$

$$\tilde{c} = \text{mass-weighted species concentration}. \tag{1.5l}$$

and C_1, C_2, C_3, C_4, C_{a1}, C_{a2}, C_b, σ_a, σ_b, σ_c, σ_ϵ, and σ_k are model parameters, i and n are directional indices, and k is the material species index. The pressure term in these equations is directly related to the material temperature through the equation of state. In turn, radiative transfer equations affect the material temperature. This is how a hydrodynamics solver, such as the BHR2 model, is coupled to a radiation solver, such as Implicit Monte Carlo.

1.2 Thermal Radiative Transfer

The thermal radiative transfer (TRT) equations are introduced for one spatial dimension ($0 \leq x \leq X$), which only requires a single angular variable, $\mu = \cos\theta$,

where θ is the angle between the particle direction and the positive x-axis. This geometry prescription is often called "slab geometry" and is made to simply represent the TRT equations. While simple, this problem geometry still allows one to adequately investigate many problems of interest. It is assumed that no scattering is present and the system is in local thermodynamic equilibrium (LTE). The LTE assumption physically represents a material that is in thermal equilibrium, emitting photons in a Planckian spectrum at the local material temperature. The equations are

$$\begin{aligned} &\frac{1}{c}\frac{\partial I}{\partial t}\left(x,\mu,\nu,t\right)+\mu\frac{\partial I}{\partial x}\left(x,\mu,\nu,t\right)+\sigma_a\left(x,\nu,T\right)I\left(x,\mu,\nu,t\right) \\ &\qquad\qquad =2\pi\sigma_a\left(x,\nu,T\right)B\left(\nu,T\right)+\frac{Q}{2}\left(x,\nu,t\right), \end{aligned} \tag{1.6a}$$

$$c_v\left(x,T\right)\frac{\partial T}{\partial t}\left(x,t\right)=\int_0^\infty\int_{-1}^1\sigma_a\left(x,\nu',T\right)\left[I\left(x,\mu',\nu',t\right)-2\pi B\left(\nu',T\right)\right]d\mu'd\nu', \tag{1.6b}$$

and have arbitrarily defined boundary conditions for $I\left(x,\mu,\nu,t\right)$ and initial conditions for $I\left(x,\mu,\nu,t\right)$ and $T\left(x,t\right)$. The terms in the TRT equations are:

$$I=ch\nu n\left(x,\mu,\nu,t\right)=\text{specific intensity}, \tag{1.7a}$$

$$n\left(x,\mu,\nu,t\right)=\text{mean number of photons per unit phase space}, \tag{1.7b}$$

$$c=299.792458\ \text{cm/sh}=\text{speed of light}, \tag{1.7c}$$

$$h=6.6260693\times10^{-35}\ \text{jk-sh}=\text{Planck's constant}, \tag{1.7d}$$

$$T=T\left(x,t\right)=\text{material temperature (keV)}, \tag{1.7e}$$

$$B = B(\nu, T) = \text{Planck's function for radiation,}$$
$$= \frac{2h\nu^3}{c^2}\left(e^{h\nu/T} - 1\right)^{-1}, \tag{1.7f}$$
$$Q = Q(x, \nu, t) = \text{isotropic photon source,} \tag{1.7g}$$
$$c_v = c_v(x, T) = \text{specific heat of material,} \tag{1.7h}$$
$$\sigma_a = \sigma_a(x, \nu, T) = \text{absorption opacity,}$$
$$= \text{(probability of absorption per unit distance).} \tag{1.7i}$$

In this system of equations all of the quantities are problem-dependent prescriptions, except for the specific intensity and the material temperature. At this point it is useful to introduce the material and radiation energy densities, U_m and U_r, respectively. They are defined as,

$$\frac{\partial U_m}{\partial T} = c_v, \tag{1.8a}$$
$$U_r = aT^4, \tag{1.8b}$$

where

$$a = \frac{8\pi^5 k^4}{15h^3c^3} = 0.01372\,\frac{\text{jk}}{\text{cm}^3\,\text{keV}^4}. \tag{1.9}$$

1.2.1 The Gray Approximation

A common approximation for the TRT equations is to integrate B, I, and Q over the entire frequency domain and assume the intensity is Planckian. This is frequently referred to as the gray approximation. Under this approximation, Eqs (1.6) become,

$$\frac{1}{c}\frac{\partial I}{\partial t}(x,\mu,t)+\frac{\partial I}{\partial x}(x,\mu,t)+\sigma_a(x)\,I(x,\mu,t)$$
$$=\sigma_a(x)\,\frac{ac}{2}T^4+\frac{Q}{2}(x,\nu,t)\,, \tag{1.10a}$$
$$c_v(x,T)\,\frac{\partial T}{\partial t}(x,t)=\int_{-1}^{1}\sigma_a(x)\left[I(x,\mu',t)-\frac{ac}{2}T^4\right]\,d\mu', \tag{1.10b}$$

when

$$I(x,\mu,t)=\int_0^\infty I(x,\mu,\nu,t)\;d\nu, \tag{1.11a}$$
$$Q(x,t)=\int_0^\infty Q(x,\nu,t)\;d\nu, \tag{1.11b}$$
$$\frac{ac}{4\pi}T^4=\int_0^\infty B(\nu,T)\;d\nu, \tag{1.11c}$$

are applied. Equations (1.10) are commonly known as the gray TRT equations and have arbitrarily-defined boundary and initial conditions for I and T.

1.3 Monte Carlo Methods

The Monte Carlo method is a widely used stochastic technique to solve complex problems in the nuclear engineering field (and many others) which are too computationally expensive to solve deterministically. MCNP is arguably one of the most widely used Monte Carlo software packages in the nuclear engineering community. In MCNP, and other Monte Carlo software, random (technically pseudorandom) numbers and probability density functions (PDFs) are used to determine where in a zone and at what energy a particle is born, in what direction it travels, how far the particle will travel before a collision, and what type of collision will occur. Depending on the collision type, the particle history is finished (due to absorption or leakage) or the particle is scattered, a new direction and length of travel are randomly gen-

erated, and the process is repeated until the particle dies (from absorption, leakage, or variance reduction techniques such as weight windows and russian roulette). This process is repeated many times to form a history, a quantity of interest (QoI) is typically tallied for this history, and many histories are run to get an average tally within some confidence interval. Effective multiplication factor k_{eff}, reaction rates, particle current through a surface, particle flux in a zone, and energy deposition in a material are typical tallies. Monte Carlo methods converge at a $1/\sqrt{n}$ rate, where n is the total number of particles. Therefore, detailed problems can even be too computationally expensive for modern supercomputing machines. For a more detailed look at Monte Carlo methods please see Refs [17, 9]

1.3.1 Implicit Monte Carlo

The Implicit Monte Carlo (IMC) method was first published by Fleck and Cummings in 1971 [4] and it approximated the photon absorption and remission process with an "effective scattering" process. This allows one to approximate the photon absorption and reemission process, which occurs on time scales typically too short to easily resolve with a temporal discretization, with a much more computationally feasible time step size. In essence, this allows one to characterize the thermal radiative transfer equations similarly to the linear neutron transport equation. However, IMC is a bit of a misnomer since all of the problem parameters are evaluated at the beginning of the time step (making it an explicit method). Following the procedure of Fleck and Cummings, the derivation begins with the gray, one-dimensional TRT equations assuming no scattering and LTE:

$$\frac{1}{c}\frac{\partial I}{\partial t} + \mu\frac{\partial I}{\partial x} + \sigma I = \frac{1}{2}\sigma acT^4, \tag{1.12a}$$

$$\frac{\partial U_m}{\partial t} = \sigma\left(\int_{-1}^{1} I\, d\mu - acT^4\right) + S. \tag{1.12b}$$

Here the only yet-to-be-defined term is S, which is an arbitrary source function. It is useful to recast these equations in terms of the radiation energy, defined in Eq. (1.8b), instead of the material temperature. Following that, it is beneficial to define

$$\frac{\partial U_m}{\partial U_r} = \beta^{-1}.$$

In the case that the material is a perfect gas with a constant specific heat, the material energy can be characterized by $U_m = bT$, where b is temperature-independent. Consequently, β becomes

$$\beta = \frac{\partial U_r}{\partial U_m} = \frac{4a^3}{b} = \frac{4U_r}{U_m}.$$

Eqs. (1.12) can be rewritten, in terms of β, as

$$\frac{1}{c}\frac{\partial I}{\partial t} + \mu\frac{\partial I}{\partial x} + \sigma I = \frac{1}{2}\sigma c U_r, \tag{1.13a}$$

$$\frac{\partial U_r}{\partial t} = \beta\sigma\left(\int_{-1}^{1} I\, u d\mu - cU_r\right) + \beta S. \tag{1.13b}$$

It is important to note that Eq. (1.13b) is now linear in β, though β is still a function of temperature; if it integrated over a time step from t^n to t^{n+1}, where $\Delta t_n = t^{n+1} - t^n$, it becomes

$$U_r^{n+1} - U_r^n = \int_{t^n}^{t^{n+1}} dt\beta\sigma \int_{-1}^{1} I\, d\mu - c\int_{t^n}^{t^{n+1}} dt\, \beta\sigma U_r + \int_{t^n}^{t^{n+1}} dt\, \beta S$$

where $U_r^n = U_r\left(x, t^n\right)$ and $U_r^{n+1} = U_r\left(x, t^{n+1}\right)$. If a time averaged function is defined as,

$$\bar{f} = \frac{1}{\Delta t_n}\int_{t^n}^{t^{n+1}} f(t)\, dt,$$

and certain parameters are factored out of the integrands in Eq. (1.3.1), it becomes

$$U_r^{n+1} - U_r^n = \Delta t_n \bar{\beta}\bar{\sigma} \int \bar{I} d\mu - c\bar{\beta}\bar{\sigma} \int_{t^n}^{t^{n+1}} dt\, U_r + \bar{\beta}\bar{S}\Delta t_n. \tag{1.14}$$

Here, Fleck and Cummings define

$$\bar{U_r} = \alpha U_r^{n+1} + (1-\alpha)\, U_r^n,$$

where α is a user-defined parameter ($\alpha \in [0.5, 1.0]$) that can vary the "implicitness" of the model. It sets the time-averaged radiation energy value as some linear combination of the current and previous time step values. This parameter is oft used in its most implicit form of $\alpha = 1$, which uses new radiation energy value as the time-averaged value. Using this approximation, Eq. (1.14) becomes

$$U_r^{n+1} - U_r^n = \Delta t_n \bar{\beta}\bar{\sigma} \left\{ \int \bar{I} d\mu - c\left[\alpha U_r^{n+1} + (1-\alpha)\, U_r^n\right] \right\} + \bar{\beta}\bar{S}\Delta t_n, \tag{1.15}$$

which further simplifies to

$$\bar{U_r} = \frac{\alpha\beta\sigma\Delta t_n}{1 + \alpha\beta c\Delta t_n \sigma} \int \bar{I} d\mu + \frac{U_r^n}{1 + \alpha\beta c\Delta t_n\sigma} + \frac{\alpha\beta\Delta t_n \bar{S}}{1 + \alpha\beta c\Delta t_n\sigma}. \tag{1.16}$$

It is commonplace to define a term that pervades the previous equations, and most other IMC equations. The *Fleck factor* is defined as

$$f = \frac{1}{1 + \alpha\beta c\Delta t_n \sigma}. \tag{1.17}$$

Implementing Eq. (1.16), in terms of f, as U_r in the right hand side of Eq. (1.13a), and making the assumption that the instantaneous specific intensity can is representative

of the time-averaged $\bar{I}$, which is a $\mathcal{O}(\Delta t)$ error, results in

$$\frac{1}{c}\frac{\partial I}{\partial t}+\mu\frac{\partial I}{\partial x}+\sigma I=\frac{\sigma}{2}\left(\alpha\beta c\Delta t_n\sigma f\right)\int I d\mu+\frac{1}{2}\left(c\sigma f U_r^n+\sigma\alpha\beta c\Delta t_n f\bar{S}\right) \tag{1.18}$$

It is important to note that the total cross section can be represented by effective absorption and scattering cross sections:

$$\sigma_a=\frac{1}{1+\alpha\beta c\Delta t_n\sigma}\sigma=f\sigma, \tag{1.19}$$

$$\sigma_s=\frac{\alpha\beta c\Delta t_n\sigma}{1+\alpha\beta c\Delta t_n\sigma}\sigma=(1-f)\,\sigma \tag{1.20}$$

A salient feature of Fleck and Cummings' work is that as $\Delta t\rightarrow\infty$, Eq. (1.18) becomes

$$\frac{1}{c}\frac{\partial I}{\partial t}+\mu\frac{\partial I}{\partial x}+\sigma I=\frac{1}{2}\sigma\int I\,d\mu+\frac{1}{2}\sigma\bar{S} \tag{1.21}$$

which, when $\bar{S}=0$, is satisfied by

$$\mu\frac{\partial I}{\partial x}+\sigma I=\frac{1}{2}\sigma\int I\,d\mu.$$

Furthermore, Eq. (1.18) is consistent because if one was to discretize Eqs. (1.12) in time, and replace I with $\bar{I}$ in all non derivative terms from the start, they would arrive at the same expression. Integrating Eq. (1.18) over direction gives

$$\frac{\partial U_m}{\partial t}=\sigma f\int I\,d\mu-c\sigma f U_r^n+f\bar{S}. \tag{1.22}$$

Temporarily deviating from the f notation allows one to describe the physical terms of Eq. (1.22):

$$\frac{\partial U_m}{\partial t} = \underbrace{\frac{\sigma}{1+\alpha\beta c\Delta t_n\sigma}\int I\,d\mu}_{\text{Absorption Heating Rate}} - \underbrace{\frac{c\sigma}{1+\alpha\beta c\Delta t_n\sigma}U_r^n}_{\text{Emission Heating Rate}} + \underbrace{\frac{1}{1+\alpha\beta c\Delta t\sigma}\bar{S}}_{\text{Source Heating Rate}}\,. \tag{1.23}$$

As $\alpha\beta c\Delta t_n\sigma \to 0$, this equation matches Eq. (1.12b) if the assumption used throughout this derivation, $\bar{U}_r = U_r$ and $\bar{S} = S$, is made. If Eq. (1.22) is integrated over a time step, the result it

$$U_m^{n+1} = U_m^n + f\sigma\int_{t^n}^{t^{n+1}} dt\int I\,d\mu - fc\Delta t_n\sigma U_r^n + f\bar{S}\Delta t_n, \tag{1.24}$$

which under the assumption that the material is a perfect gas with a constant specific heat, becomes

$$T^{n+1} = T^n + b^{-1}\left[f\sigma\int_{t^n}^{t^{n+1}} dt\int I\,d\mu - c\Delta t_n f\sigma U_r^n + f\bar{S}\Delta t_n\right]. \tag{1.25}$$

The salient takeaway from the Implicit Monte Carlo method, as noted by Fleck in Cummings in their seminal work, is that although the name implies implicitness, the final transport and energy balance solutions are entirely separate and independent.

1.4 1-D Stability Analysis

This work will begin with the model equations, Eqs. (1.4), reduced to one dimension, because the instabilities caused by Monte Carlo noise can be demonstrated in 1-D slab geometry. The one-dimensional BHR equations, along the z-direction, without the material species transport equation, are given by,

$$\frac{\partial K}{\partial t}+\frac{\partial K\tilde{w}}{\partial z}=\frac{a_z}{\bar{\rho}}\frac{\partial \bar{P}}{\partial z}-\frac{R_{zz}}{\bar{\rho}}\frac{\partial \tilde{w}}{\partial z}+\frac{\partial}{\partial z}\left(\frac{\nu_T}{\sigma_k}\frac{\partial K}{\partial z}\right)-\frac{K^{3/2}}{L}, \tag{1.26a}$$

$$\begin{aligned}\frac{\partial L}{\partial t}+\frac{\partial L\tilde{w}}{\partial z}=&\frac{L}{K}\left[\left(\frac{3}{2}-C_4\right)\frac{a_z}{\bar{\rho}}\frac{\partial \bar{P}}{\partial z}-\left(\frac{3}{2}-C_1\right)\frac{R_{zz}}{\bar{\rho}}\frac{\partial \tilde{w}}{\partial z}\right]\\&-C_3L\frac{\partial \tilde{w}}{\partial z}+\frac{\partial}{\partial z}\left(\frac{\nu_T}{\sigma_\epsilon}\frac{\partial L}{\partial z}\right)-\left(\frac{3}{2}-C_2\right)\sqrt{K},\end{aligned} \tag{1.26b}$$

$$\begin{aligned}\frac{\partial a_z}{\partial t}+\frac{\partial a_z\tilde{w}}{\partial z}=&C_{a2}\frac{b}{\bar{\rho}}\frac{\partial \bar{P}}{\partial z}-\frac{R_{zz}}{\bar{\rho}^2}\frac{\partial \bar{\rho}}{\partial z}-a_z\frac{\partial(\tilde{w}-a_z)}{\partial z}+\frac{\partial a_z^2}{\partial z}\\&+\frac{\partial}{\partial z}\left(\frac{\nu_t}{\bar{\rho}^2\sigma_a}\frac{\partial a_z}{\partial z}\right)-C_{a1}a_z\frac{\sqrt{K}}{L},\end{aligned} \tag{1.26c}$$

$$\frac{\partial b}{\partial t}+\frac{\partial b\tilde{w}}{\partial z}=2a_z\frac{\partial b}{\partial z}-2(b+1)\frac{a_z}{\bar{\rho}}\frac{\partial \bar{\rho}}{\partial z}+\bar{\rho}\frac{\partial}{\partial z}\left[\frac{\nu_T}{\bar{\rho}\sigma_b}\frac{\partial b}{\partial z}\right]-\frac{C_b\sqrt{K}}{L}b, \tag{1.26d}$$

In the presence of a constant pressure gradient ($\frac{\partial \bar{P}}{\partial z}\neq 0$) and homogenous fields ($\nabla(\cdot)=0$) Eqs. (1.26) reduce to,

$$\frac{\partial K}{\partial t}=\frac{a_z}{\bar{\rho}}\frac{\partial \bar{P}}{\partial z}-\frac{K^{3/2}}{L}, \tag{1.27a}$$

$$\frac{\partial L}{\partial t}=\frac{L}{K}\left[\left(\frac{3}{2}-C_4\right)\frac{a_z}{\bar{\rho}}\frac{\partial \bar{P}}{\partial z}\right]-\left(\frac{3}{2}-C_2\right)\sqrt{K}, \tag{1.27b}$$

$$\frac{\partial a_z}{\partial t}=C_{a2}\frac{b}{\bar{\rho}}\frac{\partial \bar{P}}{\partial z}-\frac{C_{a1}a_z\sqrt{K}}{L}, \tag{1.27c}$$

$$\frac{\partial b}{\partial t}=-\frac{C_b\sqrt{K}}{L}b. \tag{1.27d}$$

These equations model isotropic turbulent decay, but allow for the effects of a pressure gradient. Eqs. (1.28) show the physical meaning of each term in Eqs. (1.27). A simple model, such as this, is beneficial for analyzing the main production terms in the BHR model.

$$\frac{\partial K}{\partial t} = \underbrace{\frac{a_z}{\bar{\rho}}\frac{\partial \bar{P}}{\partial z}}_{\text{Production}} - \underbrace{\frac{K^{3/2}}{L}}_{\text{Dissipation}}, \tag{1.28a}$$

$$\frac{\partial L}{\partial t} = \underbrace{\frac{L}{K}\left[\left(\frac{3}{2} - C_4\right)\frac{a_z}{\bar{\rho}}\frac{\partial \bar{P}}{\partial z}\right]}_{\text{Production}} - \underbrace{\left(\frac{3}{2} - C_2\right)\sqrt{K}}_{\text{Dissipation}}, \tag{1.28b}$$

$$\frac{\partial a_z}{\partial t} = \underbrace{C_{a2}\frac{b}{\bar{\rho}}\frac{\partial \bar{P}}{\partial z}}_{\text{Production}} - \underbrace{\frac{C_{a1}a_z\sqrt{K}}{L}}_{\text{Dissipation}}, \tag{1.28c}$$

$$\frac{\partial b}{\partial t} = -\underbrace{\frac{C_b\sqrt{K}}{L}b}_{\text{Dissipation}}. \tag{1.28d}$$

After explicit time discretization the equations are,

$$\frac{K^{(n+1)} - K^{(n)}}{\Delta t} = \frac{a_z^{(n)}}{\bar{\rho}^{(n)}}\frac{\partial \bar{P}^{(n)}}{\partial z} - \frac{\left(K^{(n)}\right)^{3/2}}{L^{(n)}}, \tag{1.29a}$$

$$\frac{L^{(n+1)} - L^{(n)}}{\Delta t} = \frac{L^{(n)}}{K^{(n)}}\left[\left(\frac{3}{2} - C_4\right)\frac{a_z^{(n)}}{\bar{\rho}^{(n)}}\frac{\partial \bar{P}^{(n)}}{\partial z}\right] - \left(\frac{3}{2} - C_2\right)\sqrt{K^{(n)}}, \tag{1.29b}$$

$$\frac{a_z^{(n+1)} - a_z^{(n)}}{\Delta t} = C_{a2}\frac{b^{(n)}}{\bar{\rho}^{(n)}}\frac{\partial \bar{P}^{(n)}}{\partial z} - \frac{C_{a1}a_z^{(n)}\sqrt{K^{(n)}}}{L^{(n)}}, \tag{1.29c}$$

$$\frac{b^{(n+1)} - b^{(n)}}{\Delta t} = -\frac{C_b\sqrt{K^{(n)}}}{L^{(n)}}b^{(n)}. \tag{1.29d}$$

Solving for the updated $(n+1)$ dependent variable in each equation gives,

$$K^{(n+1)} = \Delta t \left[\frac{a_z}{\bar{\rho}} \frac{\partial \bar{P}}{\partial z} - \frac{K^{3/2}}{L} \right] + K, \tag{1.30a}$$

$$L^{(n+1)} = \Delta t \left[\frac{L}{K} \left[\left(\frac{3}{2} - C_4 \right) \frac{a_z}{\bar{\rho}} \frac{\partial \bar{P}}{\partial z} \right] - \left(\frac{3}{2} - C_2 \right) \sqrt{K} \right] + L, \tag{1.30b}$$

$$a_z^{(n+1)} = \Delta t \left[C_{a2} \frac{b}{\bar{\rho}} \frac{\partial \bar{P}}{\partial z} - \frac{C_{a1} a_z \sqrt{K}}{L} \right] + a_z, \tag{1.30c}$$

$$b^{(n+1)} = b - \Delta t \frac{C_b \sqrt{K}}{L} b, \tag{1.30d}$$

where the (n) superscripts are dropped for conciseness. The growth rate (or amplification factor) of each QoI is the ratio of the QoI evaluated at the current time step to the QoI at the previous time step: $g_f = f^{(n+1)}/f^{(n)}$. More intricate discretization methods can be performed, however the explicit Euler method provides a worst-case, bounding approximation of the maximum stable time step.

Solving for the growth rate of each QoI gives,

$$g_K = \Delta t \left[\frac{a_z}{\bar{\rho} K} \frac{\partial \bar{P}}{\partial z} - \frac{\sqrt{K}}{L} \right] + 1, \tag{1.31a}$$

$$g_L = \Delta t \left[\left(\frac{3}{2} - C_4 \right) \frac{a_z}{\bar{\rho} K} \frac{\partial \bar{P}}{\partial z} - \left(\frac{3}{2} - C_2 \right) \frac{\sqrt{K}}{L} \right] + 1, \tag{1.31b}$$

$$g_a = \Delta t \left[C_{a2} \frac{b}{\bar{\rho} a_z} \frac{\partial \bar{P}}{\partial z} - C_{a1} \frac{\sqrt{K}}{L} \right] + 1, \tag{1.31c}$$

$$g_b = 1 - \Delta t \frac{C_b \sqrt{K}}{L}. \tag{1.31d}$$

Further algebraic manipulation of Eqs. (1.31), allows for the expression of the time

step in terms of the growth factor of each QoI:

$$\Delta t_K = (g_K - 1)\left[\frac{a_z}{\bar{\rho}K}\frac{\partial \bar{P}}{\partial z} - \frac{\sqrt{K}}{L}\right]^{-1}, \tag{1.32a}$$

$$\Delta t_L = (g_L - 1)\left[\left(\frac{3}{2} - C_4\right)\frac{a_z}{\bar{\rho}K}\frac{\partial \bar{P}}{\partial z} - \left(\frac{3}{2} - C_2\right)\frac{\sqrt{K}}{L}\right]^{-1}, \tag{1.32b}$$

$$\Delta t_a = (g_a - 1)\left[C_{a2}\frac{b}{\bar{\rho}a_z}\frac{\partial \bar{P}}{\partial z} - C_{a1}\frac{\sqrt{K}}{L}\right]^{-1}, \tag{1.32c}$$

$$\Delta t_b = \frac{L\,(1 - g_b)}{C_b\sqrt{K}}. \tag{1.32d}$$

Upon inspection of Eqs. (1.32a) - (1.32c), it is easy to see that the denominator must be negative for the time step to remain positive with a bound growth rate (where $|g| < 1$). For Eq. (1.32d), so long as the growth rate is bound ($|g| < 1$), the time step will be larger than zero. Consequently, the maximum stable time step is given by $t = \min(\Delta t_K, \Delta t_L, \Delta t_a, \Delta t_b)$. The stability of this system depends on the dissipation terms (those with $\sqrt{K}/L$) being larger than the production terms (those with the pressure gradient). If this occurs, the denominator remains negative and a stable time step is realized. However, if the signs of a_z and the pressure gradient oppose one another, the production term can cause the denominator to become positive, in which an unphysical (negative) time step is required. Therefore, the salient point is that a_z and $\partial \bar{P}/\partial z$ pointing in the same direction guarantees stability. This task is made much more difficult by stochastic noise in the pressure term, which is exacerbated by a gradient via finite difference, causing the direction of the pressure gradient to incorrectly flip directions (contrary to the flow of material - the sign of a_z). Noise reduction in the energy density results of the Implicit Monte Carlo simulation, which directly feeds into the BHR-2 pressure term, is critical in increasing the robustness of the coupled system.

1.4.1 Filtering the Pressure Term

If it is not possible to reduce the error in the stochastic IMC process, a logical solution to reducing the noise in the pressure term would be to filter it as it passes from the radiation solve (IMC) to the hydrodynamics solve (BHR-2). There are a myriad of filter options, but three popular choices are the mean, median, and Gaussian filters.

The mean filter can be expressed as a convolution. Let $f(x, y, z)$ be an arbitrary function and

$$g(x, y, z) = \begin{cases} \dfrac{1}{(2a)^3} & |x| \leq a,\ |y| \leq a,\ |z| \leq a, \\ 0 & \text{otherwise,} \end{cases} \tag{1.33}$$

therefore the convolution of $g(x, y, z)$ is

$$(f * g)(x, y, z) = \int_{x-a}^{x+a} dx' \int_{y-a}^{y+a} dy' \int_{z-a}^{z+a} dz' \frac{1}{2a^3} f(x', y', z'). \tag{1.34}$$

Alternatively, the Gaussian filter can also be represented as a convolution by defining

$$g(x, y, z) = \frac{1}{(2\pi)^{3/2}\,\sigma^3} \exp\left(-\frac{x^2 + y^2 + z^2}{2\sigma^2}\right). \tag{1.35}$$

Thus, as a convolution the Gaussian filter is given by

$$(f * g)(x, y, z) = \int_{-\infty}^{\infty} dx' \int_{-\infty}^{\infty} dy' \int_{-\infty}^{\infty} dz' \frac{1}{(2\pi)^{3/2}\,\sigma^3} \exp\left(-\frac{x^2 + y^2 + z^2}{2\sigma^2}\right) f(x', y', z'). \tag{1.36}$$

Nevertheless, the median filter cannot be represented as convolution. As such, collapsing the Gaussian and mean filters down to one dimension allows you to qualitatively compare the three filters. The mean filter takes a value and its two neighbors and replaces that value with the mean of itself and its neighbors. The median is the

same process except the value is replaced by the median of itself and its neighbors, instead of the mean. The Gaussian filter takes a subset of data, possible a value and its neighbors, and calculates the mean and standard deviation for the subset, and represents it with a normal distribution. These three filters are used to filter the pressure term generated from material temperature data exported from RAGE for a CH/Al interface problem that exhibits very noisy behavior. This behavior is illustrated in Fig 1.1.

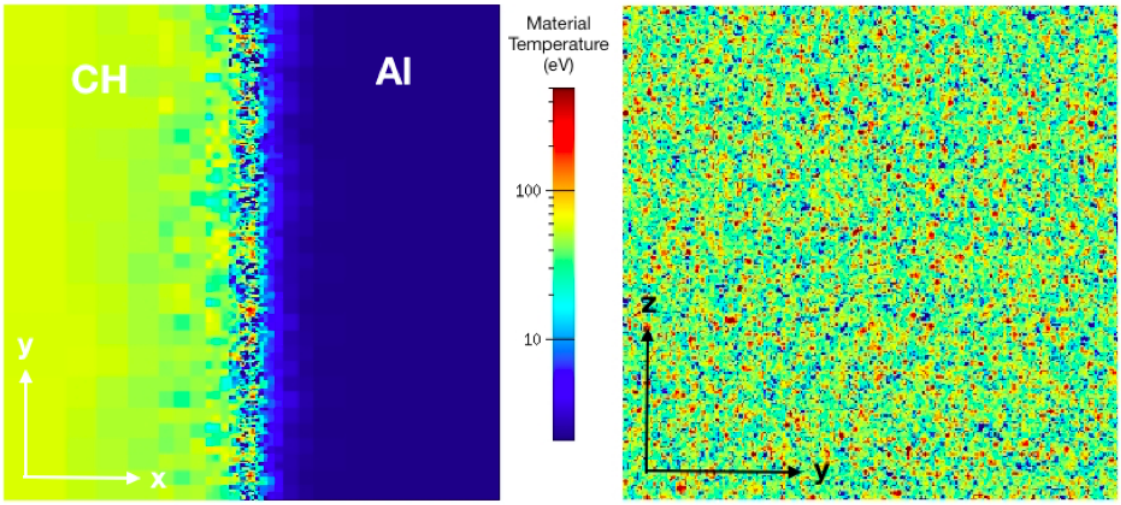

Figure 1.1: Material temperature, as calculated by RAGE, at the interface of Al/CH [10].

The material temperature is updated following the IMC solve via the material energy balance equation. It relates to the pressure, P, by

$$P = (\gamma - 1)\,\rho c_v T, \tag{1.37}$$

where a is the radiation energy density constant, as defined in Eq. 1.9, $\gamma = 1.4$, and

$\rho c_v = 0.3$ GJ/cm^3-keV. Using this formulation, a lineout of the pressure at $x = 0.001$ cm in Fig. 1.1 is given in Fig. 1.2. Clearly, the data is very noisy. Figure 1.3 shows that the noise is exacerbated when the gradient is estimated with a simple finite difference. Throughout this thesis, the only finite difference method investigated uses a simple central finite difference stencil. Not only is the noise exacerbated, but the gradient oscillates around zero, leading to a number of sign changes (which were shown to be a driver of instability earlier).

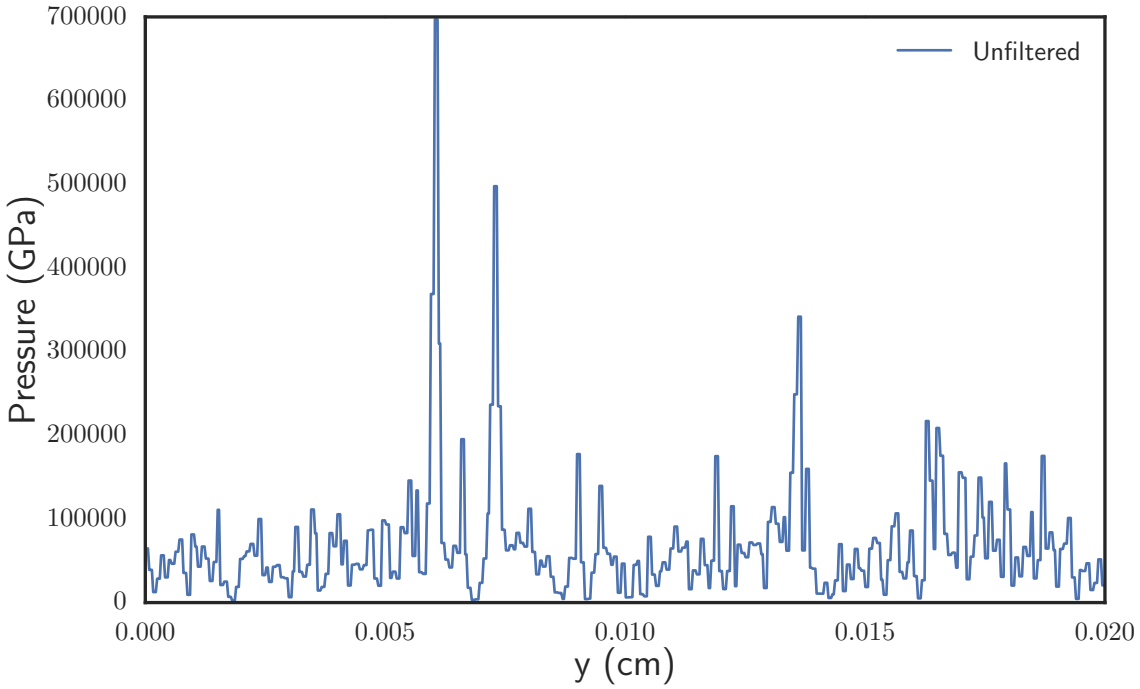

Figure 1.2: Unfiltered pressure lineout at $x = 0.001$ cm.

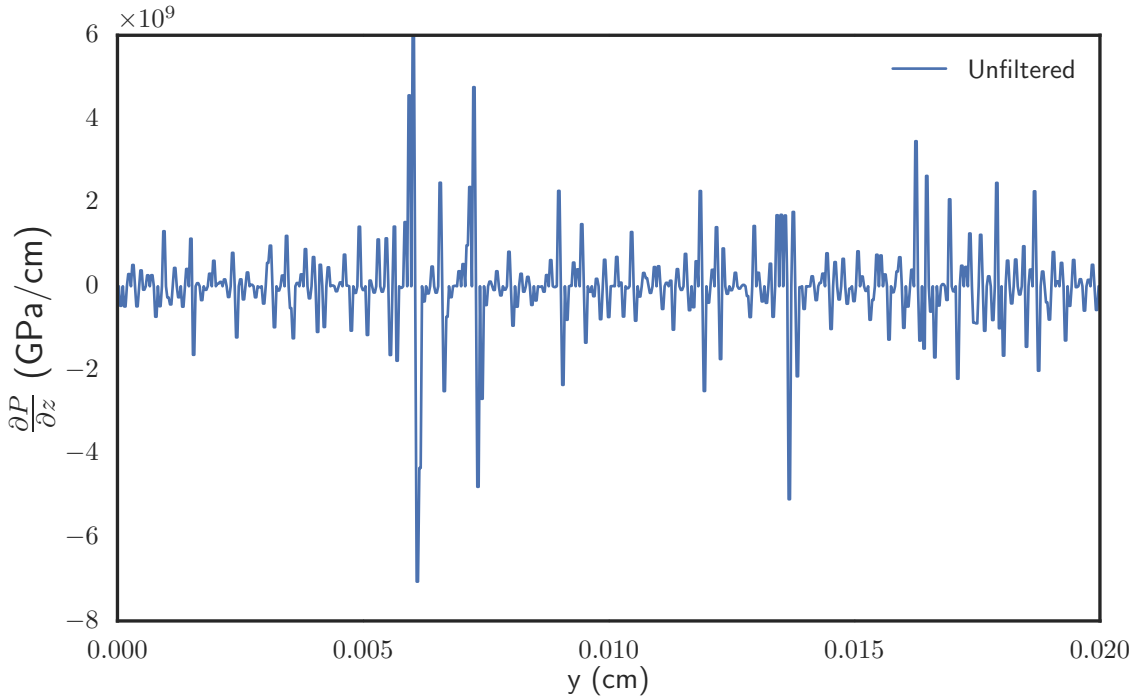

Figure 1.3: Unfiltered pressure gradient lineout at $x = 0.001$ cm.

Applying the filters mentioned above could alleviate this issue. Figure 1.4 shows the pressure gradient after one application of the mean, median, and gaussian filters, in comparison to the unfiltered gradient. The median filter drastically reduced the spikes while the mean and gaussian filters reduced the peaks, but not as drastically. Recursively applying these filters, could further reduce the noise, to an acceptable level. Figure 1.5 shows the pressure gradient after 100 applications of all three filters, compared to the unfiltered gradient. The median profile has hardly changed from the single application, however the mean and the gaussian profiles are now substantially reduced. Table 1.1 shows a summary of the pressure gradient profiles are recursive applications of linear filters. The maximum of the pressure gradient is shown because of its importance in the BHR-2 time step determination and the mean of the pressure gradient is shown as a surrogate of the data lost in the filtering process. If the mean

changes drastically during the filtering process, is the filtered data really providing an accurate, but less noisy, picture of the unfiltered data?

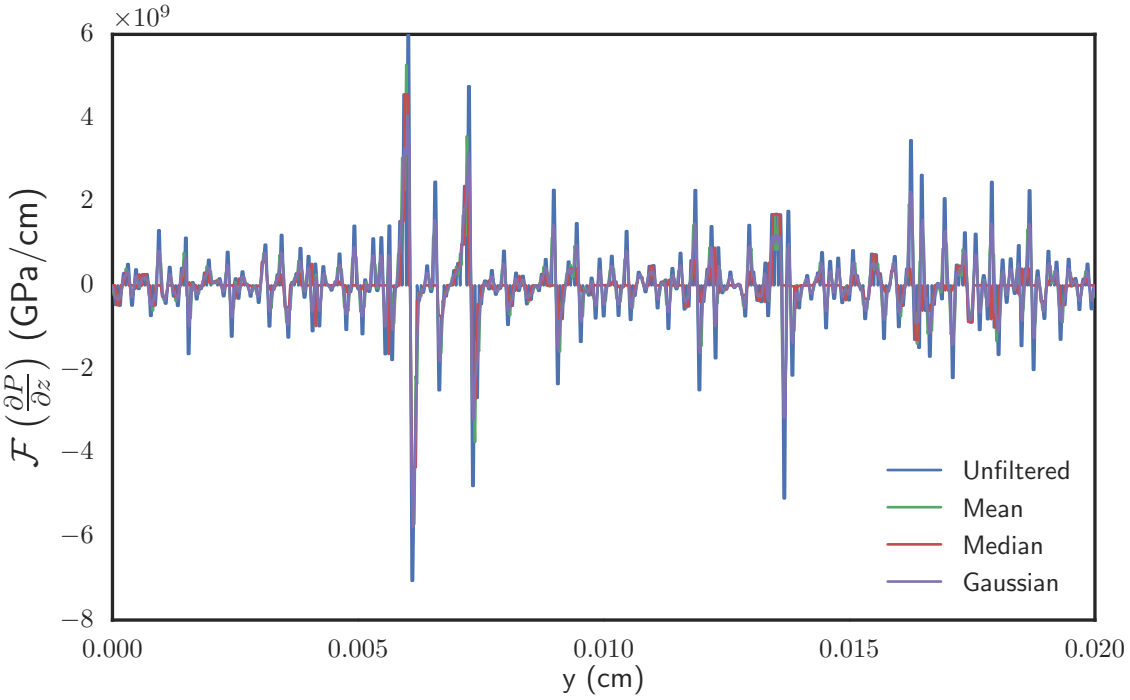

Figure 1.4: Pressure gradient after 1 filter: $\mathcal{F}(\nabla P)$.

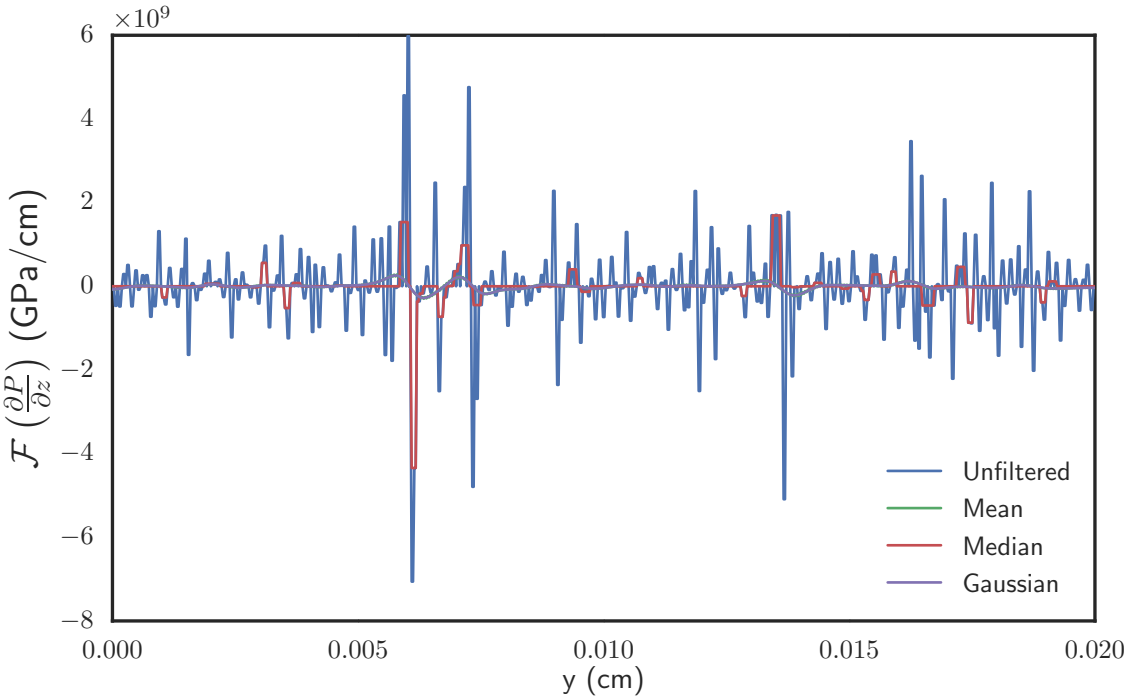

Figure 1.5: Pressure gradient after 100 recursive filters: $\mathcal{F}(\nabla P)$.

Upon inspection of Table 1.1, it is apparent that filtering can severely maim the original data. For example, with 100 recursive applications of the mean filter, the mean of the data changed 134% by filtering prior to the gradient, but changes less than 0.01% if filtered after the gradient. This is in direct contrast to the median filter characteristics which resulted in the exact opposite (negligible change in the mean for filtering after the gradient, drastic change when filtering prior).

Table 1.1: Effects of recursive linear filters on pressure data from RAGE.

Type	Number	$\mathcal{F}(P)$		$\nabla\mathcal{F}(\nabla P)$	
		Maximum	Mean	Maximum	Mean
Mean	1	5.272E+09	-5.911E+06	5.272E+09	-2.190E+06
	5	3.122E+09	1.981E+07	3.122E+09	-2.190E+06
	10	2.173E+09	1.157E+07	2.173E+09	-2.190E+06
	25	1.081E+09	1.008E+07	1.081E+09	-2.190E+06
	100	2.390E+08	7.538E+05	2.807E+08	-2.190E+06
Median	1	4.563E+09	-2.200E+06	4.563E+09	-4.653E+06
	5	4.563E+09	-2.199E+06	1.692E+09	7.261E+05
	10	4.563E+09	-2.199E+06	1.692E+09	7.261E+05
	25	4.563E+09	-2.199E+06	1.692E+09	7.261E+05
	100	4.563E+09	-2.199E+06	1.692E+09	7.261E+05
Gaussian	1	4.067E+09	-3.737E+06	4.067E+09	-2.190E+06
	5	2.721E+09	-8.692E+05	2.721E+09	-2.190E+06
	10	1.956E+09	-6.128E+05	1.956E+09	-2.190E+06
	25	1.007E+09	-1.080E+06	1.007E+09	-2.190E+06
	100	2.595E+08	-4.888E+05	2.595E+08	-2.190E+06

Unfiltered: Maximum = 5.9803E+09, Mean = -2.1897E+06

The maximum pressure gradient directly corresponds to the maximum time step, as shown in Eqs. (1.32). The growth factor, g, affects the magnitude of the time step size, but does not affect the changes in the size due to the pressure gradient, so long as it is consistent throughout. Consequently, the best-case scenario of $g = -1$, rapid decay of the QoI's, is chosen to illustrate how the maximum pressure gradient can change the maximum stable time step in the BHR-2 system. To do this, BHR-2 model parameters are chosen following Stalsberg-Zarling's recommendations [15], shown in Table 1.2, and Eqs. (1.32) are solved for the maximum stable time step using the maximum pressure gradients shown in Table 1.1. The results are shown in Table 1.3 where the Pct. Increase columns indicate the percent increase in the time step size, compared to the unfiltered time step.

Table 1.2: BHR model parameter values (from Ref. [15]).

K	L	a_z	C_2	C_4	C_{a1}	C_{a2}	ρ	b	C_b
0.001	0.5	0.001	1.92	1.05	6.0	1.0	1.0	0.06	2.5

Table 1.3: Effects of recursive linear filters on the BHR-2 time step size.

Type	Number	$\nabla\mathcal{F}(P)$		$\mathcal{F}(\nabla P)$	
		Δt	Pct. Increase	Δt	Pct. Increase
Mean	1	6.32271E-12	113%	6.32271E-12	113%
	5	1.06769E-11	192%	1.06769E-11	192%
	10	1.53398E-11	275%	1.53398E-11	275%
	25	3.08356E-11	553%	3.08356E-11	553%
	100	1.39470E-10	2502%	1.18751E-10	2130%
Median	1	7.30514E-12	131%	7.30514E-12	131%
	5	7.30514E-12	131%	1.97006E-11	353%
	10	7.30514E-12	131%	1.97006E-11	353%
	25	7.30514E-12	131%	1.97006E-11	353%
	100	7.30514E-12	131%	1.97006E-11	353%
Gaussian	1	8.19605E-12	147%	8.19605E-12	147%
	5	1.22504E-11	220%	1.22504E-11	220%
	10	1.70416E-11	306%	1.70416E-11	306%
	25	3.31016E-11	594%	3.31016E-11	594%
	100	1.28452E-10	2305%	1.28452E-10	2305%

Unfiltered: $\Delta t = 5.57386\text{E-}12$

2. COUPLING BHR-2 AND IMC

2.1 The Issues of Coupling BHR2 and IMC in Practice

A commonly-run problem, which also exhibits the drawback of coupling BHR-2 and IMC, was run in the RAGE radiation-hydrodynamics code (Radiation Adaptive Grid Eulerian) [6]. This problem consists of a 0.03 cm cube with 0.002275 cm aluminum foil on the right hand side. To to the left of the aluminum exists 0.0275 cm of CH foam, while to the right of the foil is a 400 eV source. This problem was run with Implicit Monte Carlo with 102 groups and only 100 particles per time step, as well as gray diffusion. Furthermore, it was run with both transport methods with both no mix and BHR-2 mix model. When the turbulent kinetic energy parameter in the BHR-2 model is set sufficiently high (5×10^5 ergs/cm), the problem proceeds through time and the BHR-2 model damps some of the noise present in the no mix results. This is shown in Fig. 2.1.

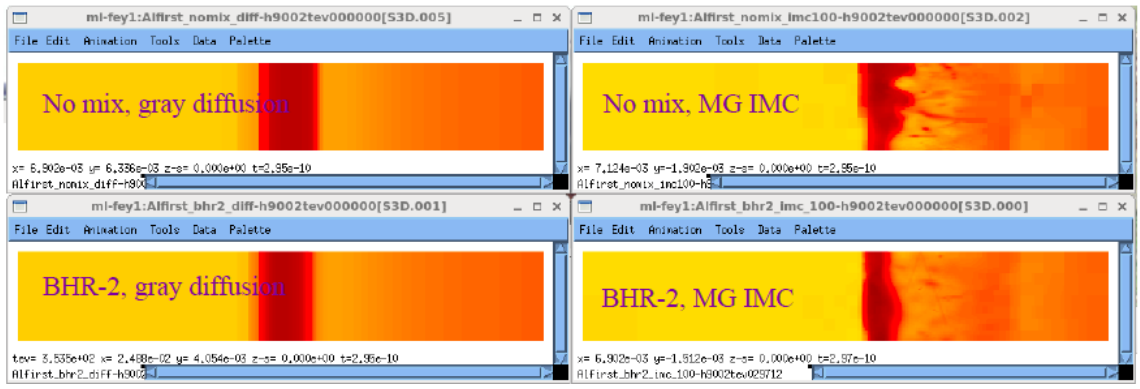

Figure 2.1: RAGE Radiation-hydrodynamics code highlighting BHR-2 damping some of the noise present with no mix model when the turbulent kinetic energy is set sufficiently high [10].

Figure 2.1 shows a readout at $t = 2.9 \times 10^{-10}$ seconds and shows that the gray diffusion results look very smooth and BHR-2 has little effect, however it is missing the turbulent mixing that is known to occur at those material interfaces. The multi-group IMC captures this turbulent mixing, at the expense of have too much mixing. The drastic variation in shock interface in the no mix, IMC case is likely caused by the low number of particles, however BHR-2 damps this noise to an extent as shows a non-uniform, but cohesive shock front, even with only 100 particles. Unfortunately, this is not the case when the turbulent kinetic energy is not set sufficiently high. Figure 2.2 shows the same problem as before, but with $K = 1.0$ ergs/cm. The left panel of the figure shows that at $t = 3.41 \times 10^{-12}$ seconds, the gray diffusion and BHR-2 model with 100,000 IMC particles show smooth results. The noise caused by IMC is present in the lower lefthand panel, where the results are not so smooth for only 100 IMC particles. From this, one might say *problem solved*; just use 100,000 particles and the noise is gone. Unfortunately, by inspecting the right panel, one can see that this does not solve the problem. It helps, since 100,000 particles makes it further before crashing (1.65×10^{-11} vs. 1.11×10^{-11} seconds), but in the end they both crash while the gray diffusion method with BHR-2 runs to completion. These two problem runs confirm what was shown in the stability analysis section: coupling BHR-2 and IMC works for some, but not all, problems. A prescription for the gradient of the energy density could alleviate the noise application properties of finite difference methods on the radiation pressure term, which couples to the BHR-2 model, but not diffusion.

2.2 Energy Density Estimator

As shown by the filtering results, finite difference methods are susceptible to noise. Another popular approximation technique is finite elements. A first-order finite

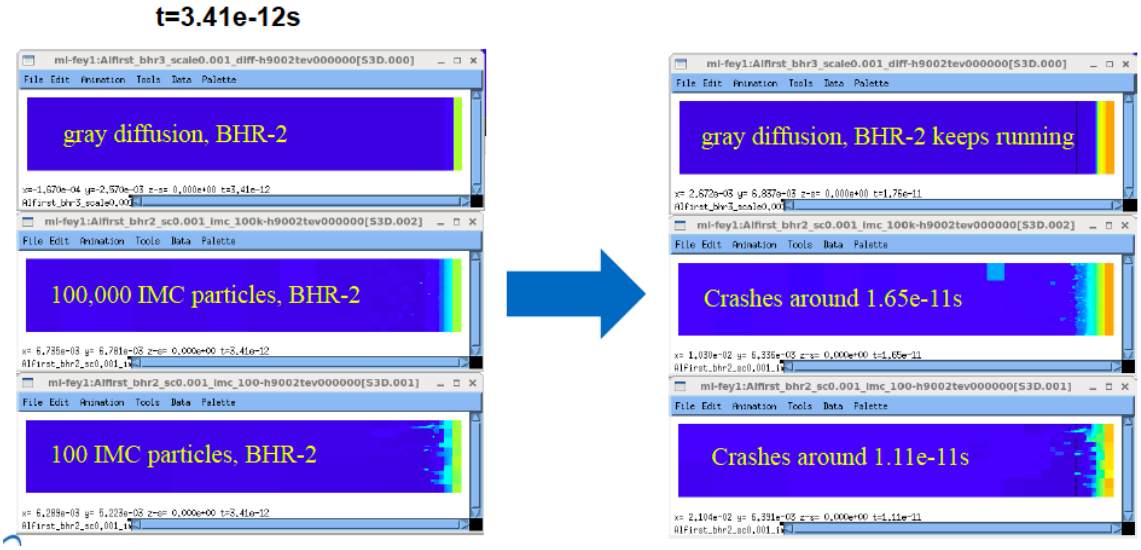

Figure 2.2: RAGE Radiation-hydrodynamics code crashing using BHR-2 when coupled to IMC, but not with gray diffusion when the turbulent kinetic energy is low [10].

element representation of the radiation energy in a zone, E, can be approximated as

$$E(\mathbf{r}) = E(x, y, z) = a_0 + a_1(x - x_c) + a_2(y - y_c) + a_3(z - z_c), \tag{2.1}$$

where the a coefficients have units of energy per length, x, y, z define the particle position and x_c, y_c, z_c define the center of the zone. These positions can also be represented in vector format: $\mathbf{r}$ and $\mathbf{r_c}$, respectively. The a_i coefficients represent the directional gradients of the zone energy. Integrating over all space against a basis function in each direction, which represents the energy absorbed in each direction,

results in

$$\int_{x_L}^{x_R} dx \int_{y_L}^{y_R} dy \int_{z_L}^{z_R} dz \; (x - x_c) \left[a_0 + a_1 (x - x_c) + a_2 (y - y_c) + a_3 (z - z_c) \right] = \frac{a_1}{12} \Delta x^3, \tag{2.2a}$$

$$\int_{x_L}^{x_R} dx \int_{y_L}^{y_R} dy \int_{z_L}^{z_R} dz \; (y - y_c) \left[a_0 + a_1 (x - x_c) + a_2 (y - y_c) + a_3 (z - z_c) \right] = \frac{a_2}{12} \Delta y^3, \tag{2.2b}$$

$$\int_{x_L}^{x_R} dx \int_{y_L}^{y_R} dy \int_{z_L}^{z_R} dz \; (z - z_c) \left[a_0 + a_1 (x - x_c) + a_2 (y - y_c) + a_3 (z - z_c) \right] = \frac{a_3}{12} \Delta z^3, \tag{2.2c}$$

where $\Delta x = x_R - x_L$, $\Delta y = y_R - y_L$, and $\Delta z = z_R - z_L$ are the zone dimensions. In order to relate these quantities to a particle history, one must integrate the energy lost by the particle (absorbed in the material) over its path against a basis function in each direction. This is given by

$$\int_0^s ds' \; \left[x (s') - x_c \right] E_0 e^{-\sigma s'} = -\frac{E_0}{\sigma} \left[\Omega_x s e^{-\sigma s} + \left(\frac{\Omega_x}{\sigma} + (x_0 - x_c) \right) \left(e^{-\sigma s} - 1 \right) \right], \tag{2.3a}$$

$$\int_0^s ds' \; \left[y (s') - y_c \right] E_0 e^{-\sigma s'} = -\frac{E_0}{\sigma} \left[\Omega_y s e^{-\sigma s} + \left(\frac{\Omega_y}{\sigma} + (y_0 - y_c) \right) \left(e^{-\sigma s} - 1 \right) \right], \tag{2.3b}$$

$$\int_0^s ds' \; \left[z (s') - z_c \right] E_0 e^{-\sigma s'} = -\frac{E_0}{\sigma} \left[\Omega_z s e^{-\sigma s} + \left(\frac{\Omega_z}{\sigma} + (z_0 - z_c) \right) \left(e^{-\sigma s} - 1 \right) \right], \tag{2.3c}$$

where σ is the zone's opacity and the particle begins at position $\mathbf{r_0} = (x_0, y_0, z_0)$ with an initial energy E_0 and travels along $\mathbf{\Omega} = (\Omega_x, \Omega_y, \Omega_z)$ for a distance (also known as a step length) s. This derivation assumes the popular implicit capture technique, in which a particle's weight is reduced by the fraction of particles which

scatter instead of undergoing absorption. Relating the particle history to the finite element representation by combining Eqs. (2.2) with Eqs. (2.3), followed by some algebraic manipulation, results in

$$\frac{\partial U(\mathbf{r})}{\partial x} = a_1 = \frac{12E_0}{\sigma V(\Delta x)^2}\left[\Omega_x - (\Omega_x + \sigma\Omega_x s + \sigma(x_0 - x_c))\exp(-\sigma s) + \sigma(x_0 - x_c)\right], \tag{2.4a}$$

$$\frac{\partial U(\mathbf{r})}{\partial y} = a_2 = \frac{12E_0}{\sigma V(\Delta y)^2}\left[\Omega_y - (\Omega_y + \sigma\Omega_y s + \sigma(y_0 - y_c))\exp(-\sigma s) + \sigma(y_0 - y_c)\right], \tag{2.4b}$$

$$\frac{\partial U(\mathbf{r})}{\partial z} = a_3 = \frac{12E_0}{\sigma V(\Delta z)^2}\left[\Omega_z - (\Omega_z + \sigma\Omega_z s + \sigma(z_0 - z_c))\exp(-\sigma s) + \sigma(z_0 - z_c)\right], \tag{2.4c}$$

where $U(\mathbf{r})$ is the energy density in the zone and V is the zone volume. For implementation into a Monte Carlo code which is discretized in time, Eqs. (2.4) represent the change to the energy density during that time step. The estimator, in vector form, is given by

$$\begin{pmatrix} \text{Absorbed} \\ \text{Energy Density} \\ \text{Rate Gradient} \end{pmatrix} = c\sigma\nabla U(\mathbf{r}) = \frac{12cU_0}{(\Delta\mathbf{r})^2}\left[\boldsymbol{\Omega} - (\boldsymbol{\Omega} + \sigma\boldsymbol{\Omega}s + \sigma(\mathbf{r_0} - \mathbf{r_c}))\exp(-\sigma s) + \sigma(\mathbf{r_0} - \mathbf{r_c})\right], \tag{2.5}$$

where $\Delta\mathbf{r} = (\Delta x, \Delta y, \Delta z)$. The right hand side of Eq. (2.5) has units of $energy/(volume - length - time)$, which represent the gradient of the energy absorption rate density (as shown on the left hand side).

3. RESULTS

3.1 The FINMCOOL IMC Code

FINMCOOL is an Implicit Monte Carlo code, written in C++, which was developed at Texas A&M University. It currently can solve 3-D grey transport problems, on either a cartesian or cylindrical grid, for multiple immiscible materials. Additionally, it has several variance reduction techniques (weight windows, implicit capture, roulette, etc.) and source tilting. An important feature of FINMCOOL is that it allows for setting of the random number seed. Consequently, running the same simulation with different random number seeds allows for an ensemble average and standard deviation in the results to be taken. This allows for direct comparison of the variance of gradient estimation methods. The output from FINMCOOL consists of `.silo` and `.txt` files, of which the `.txt` files are parsed using Python and visualized in Visit.

3.2 1-D Pure Absorber Problem

Verification is an important process in code development. Verification is used to test if the software (or a new capability of the software) performs how the developers expect. For example, this can be accomplished by verify convergence rates as meshes are refined. *Verification does not prove the accuracy of the software.* FINMCOOL has a test suite which routinely performs verification tests for existing capabilities. For new capabilities, such as the gradient estimator, verification tests must be prescribed and confirmed before being implemented. For the gradient estimator, a one-dimensional, pure absorber problem with a boundary source was selected as a verification problem. The problem was set up as a pure absorber by setting the single material to have an extremely large c_v which effectively makes it improbable for

the material to re-emit absorbed energy (remember re-emission of absorbed energy is how IMC models photon scattering). Because of the problem's simplicity, an analytical solution to the particle intensity (and consequently the energy density) can be found. The derivation starts with the 1-D steady-state transport equation, with no scattering or source term,

$$\mu \frac{\partial I(\mu, x)}{\partial x} + \sigma I(\mu, x) = 0, \tag{3.1}$$

for $x \in [0, \ell]$ and $\mu = \cos\theta \in [-1, 1]$ where θ is the angle between the particle direction and the positive x-axis. The boundary conditions,

$$I(\mu, 0) = \frac{acT^4}{2}, \quad 0 < \mu \leq 1,$$
$$I(\mu, \ell) = 0, \quad -1 \leq \mu < 0,$$

are also imposed, where a and c are the radiation constant and the speed of light, respectively. Equation (3.1) is solved by

$$I(\mu, x) = C \exp\left(-\frac{\sigma}{\mu} x\right). \tag{3.2}$$

Integrating Eq. (3.2) over all positive angles gives,

$$\sigma U(x) = C \int_0^1 d\mu \, \exp\left(-\frac{\sigma}{\mu} x\right) = C \mathrm{E}_2(\sigma x), \tag{3.3}$$

where E_2 is the second-order exponential integral function. Taking the derivative of this solution gives,

$$\frac{\partial}{\partial x} \sigma c U(x) = -\sigma^2 C \mathrm{E}_1(\sigma x) = -\sigma^2 \frac{acT^4}{2} \mathrm{E}_1(\sigma x), \tag{3.4}$$

where E_1 is a first-order exponential integral function. With this analytical solution, the accuracy of the estimator can be determined for this simple problem. Furthermore, by running many different cases of this problem, a verification study can be performed since the tally should become more accurate as the time and space grids are refined. The 15 cases which were performed span different combinations of time step sizes (Δt), grid spacing (Δx), and material opacities (σ). These cases allow for direct comparison of the benefits of the estimator over typical finite difference methods. However, the stochastic noise should be almost negligible due to the problem's simplicity. As a consequence of this, the reduction in solution variance with the estimator, versus finite difference, may be low.

Fifteen different cases of the 1-D absorber problem were performed. The varied parameters were prescribed by: Δt = (0.001, 0.005, 0.01) s, Δx = (0.01, 0.01) cm (Note: ℓ = 1 cm), and σ = (1, 2, 10) cm^{-1}. Each case was run with 20 different random number seeds to gather a mean and variance for both gradient calculation methods. The results from both methods, with each seed, were compared to the analytic solution for the case. Across all 300 runs, the estimator results had a average variance 0.4% larger than the finite difference results. Nevertheless, the error (when compared to the analytic solution) from the mean finite difference results was up to 1013% larger than the mean estimator results. This shows a drastic improvement from the finite difference method to the estimator method, with only a slight increase in the variance (which is expected to decrease as the problem complexity increases). The average error in the estimator ranged from 0.2 - 3.6%, compared to 0.4 - 40.1% for the finite difference method. The estimator errors decrease as the grid is refined; the most accurate case had Δt = 0.05 s, Δx = 0.001 cm, and σ = 2 cm^{-1}. This demonstrates a successful verification test. Overall, this simple problem provided tremendous insight, as well as confidence in the estimator. That being said, the one

downside was the lack of variance reduction.

The mean percent error (MPE) and the mean percent standard deviation (MPSD) for all fifteen cases are summarized in Table 3.1. The two rightmost columns show the differences in MPE and MPSD between the estimator and the finite difference methods. A positive number represents an increase in the error or variance in the estimator when compared to the finite difference, and a negative value represents a reduction in the error or variance. Generally speaking, the goal for the estimator would be to reduce both the error and the variance of the method. However, over the fifteen cases, the error is reduced, sometimes substantially, at the expense of a slight increase in the mean percent standard deviation of the results.

Something to recognize is that the results do not change substantially as the time step changes (row by row). This may be caused by the three Δt values are situated on a plateau and a much smaller time step could yield different behavior. In addition, there is little difference between $\sigma = 1$ and $\sigma = 2$, however $\sigma = 10$ yields quite different results. Because of this, it may be beneficial to investigate more optically thick zones.

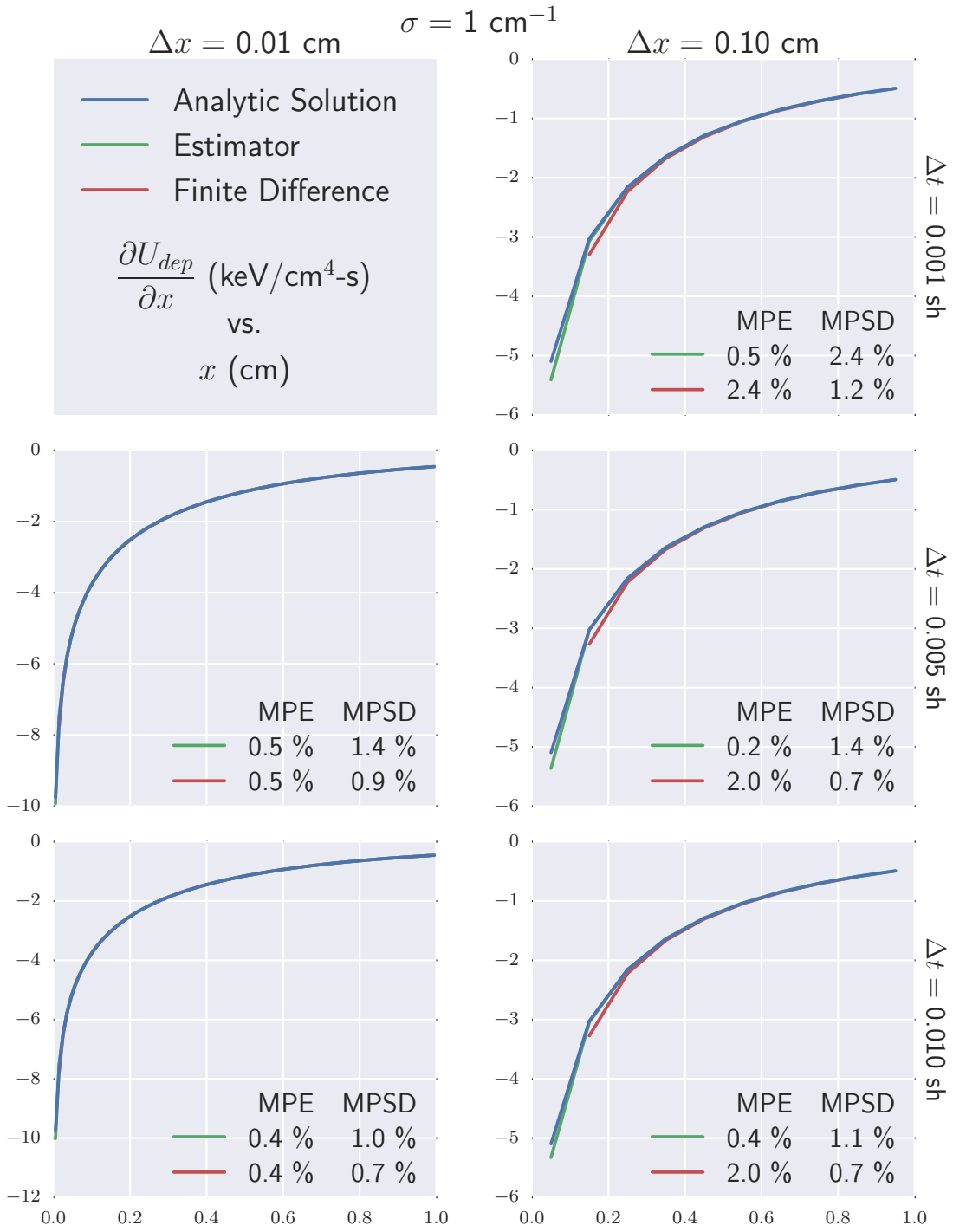

Figure 3.1: Net Deposited Energy Density Gradient for 1-D Absorber problems with $\sigma = 1$ cm^{-1} where MPE is the mean percent error and MPSD is the mean percent standard deviation.

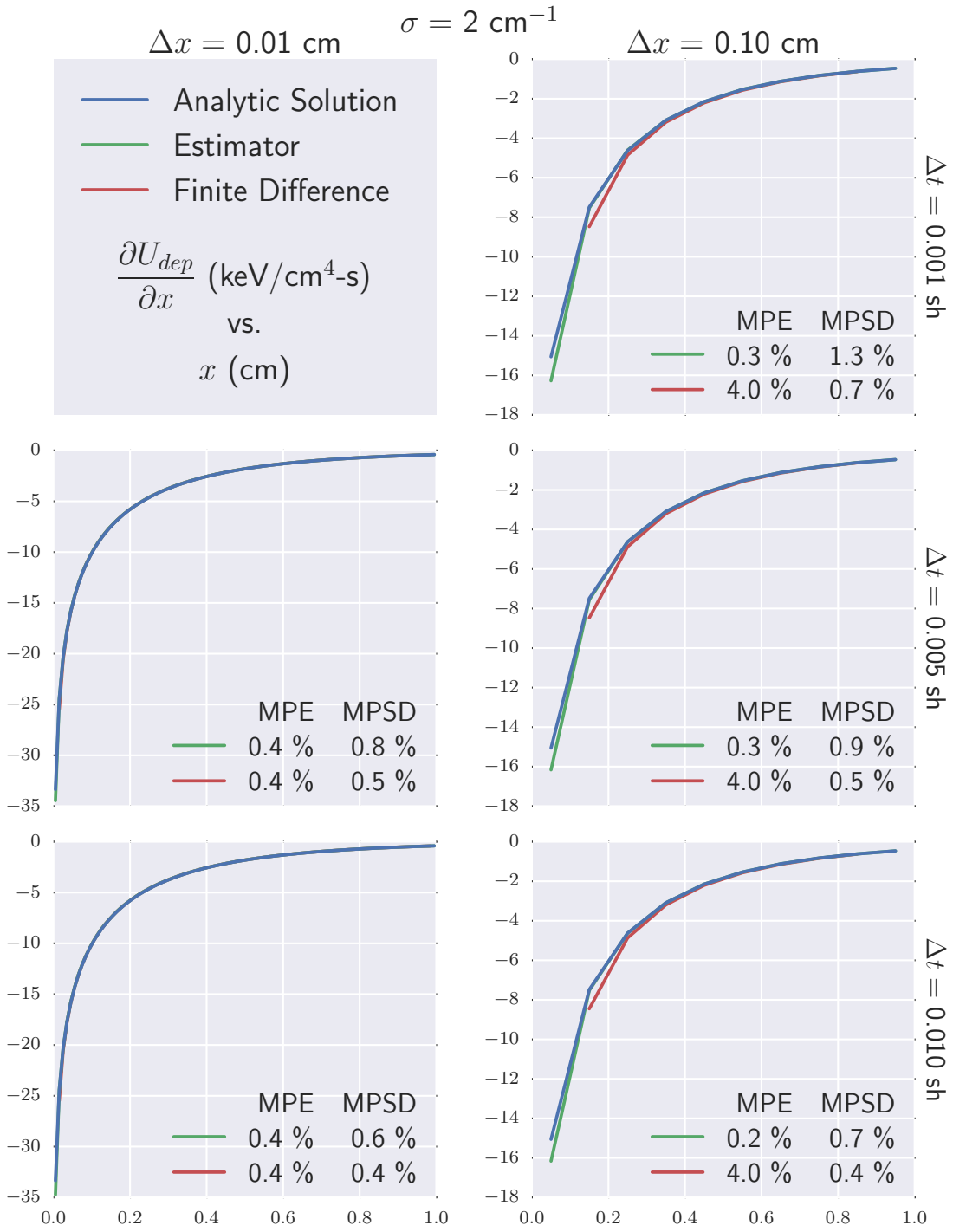

Figure 3.2: Net Deposited Energy Density Gradient for 1-D Absorber problems with $\sigma = 2$ cm^{-1} where MPE is the mean percent error and MPSD is the mean percent standard deviation.

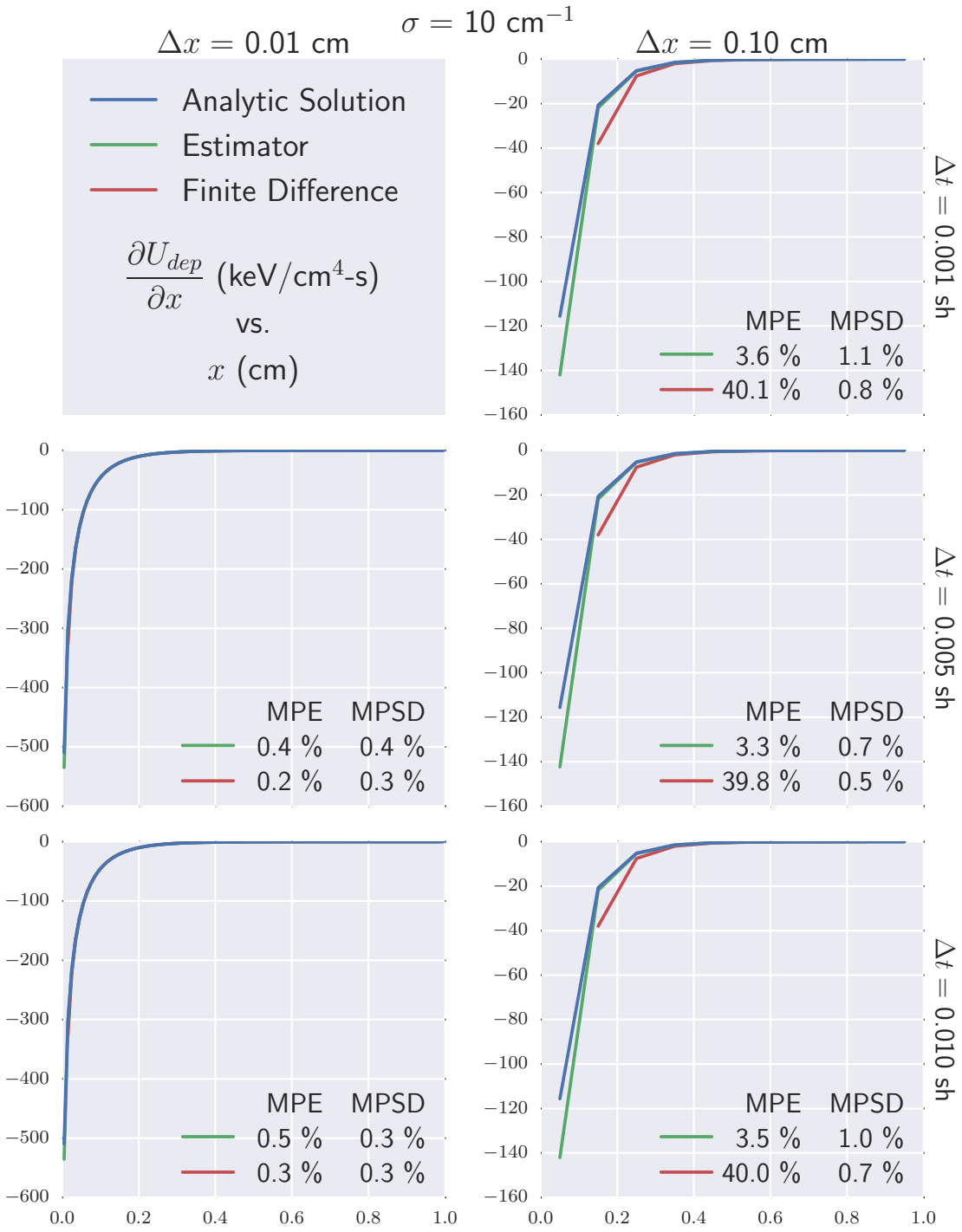

Figure 3.3: Net Deposited Energy Density Gradient for 1-D Absorber problems with $\sigma = 10$ cm^{-1} where MPE is the mean percent error and MPSD is the mean percent standard deviation.

Table 3.1: Summary of 1-D Absorber results.

Δx	Δt	σ	Estimator		Finite Difference		E - FD	
(cm)	(sh)	(cm^{-1})	MPE	MPSD	MPE	MPSD	MPE	MPSD
	0.01	0.005	0.5	1.4	0.5	0.9	0.0	0.5
	0.01	0.010	0.4	1.0	0.4	0.7	0.0	0.3
1	0.10	0.001	0.5	2.4	2.4	1.2	-1.9	1.2
	0.10	0.005	0.2	1.4	2.0	0.7	-1.8	1.3
	0.10	0.010	0.4	1.1	2.0	0.7	-1.6	0.4
	0.01	0.005	0.4	0.8	0.4	0.5	0.0	0.3
	0.01	0.010	0.4	0.6	0.4	0.4	0.0	0.2
2	0.10	0.001	0.3	1.3	4.0	0.7	-3.7	0.6
	0.10	0.005	0.3	0.9	4.0	0.5	-3.7	0.4
	0.10	0.010	0.2	0.7	4.0	0.4	-3.8	0.3
	0.01	0.005	0.4	0.4	0.2	0.3	0.2	0.1
	0.01	0.010	0.5	0.3	0.3	0.3	0.2	0.0
10	0.10	0.001	3.6	1.1	40.1	0.8	-36.5	0.3
	0.10	0.005	3.3	0.7	39.8	0.5	-36.5	0.2
	0.10	0.010	3.5	1.0	40.0	0.7	-36.5	0.3

3.3 2-D Tophat Problem

The so-called "tophat" problem contains an area of optically thick material which surrounds a path of optically thin material that surround an optically thick island. A source is located on the left plane of the optically thin region of Fig. 3.4. This is a popular benchmark problem in thermal radiation transport and even though it lacks an analytical solution, the absorbed energy density gradient can be qualitatively evaluated. At very early times, there will be large gradients near the source at the material interface, which point toward the center of the optically thin region. As the time progresses, and the particles stream to the right, the gradients will follow down the material interfaces still pointing toward the middle of the optically thin region. As the particles begin to stream into the optically thick island, the gradient

at that material interface will point toward the island, where more particles are being absorbed. This is the type of behavior expected from the estimator implementation. The problem is run with 20 different random number seeds, similar to the 1-D absorber problem, and the results from FINMCOOL are output as `.txt` files. They are read into a Python script which calculates the time-dependent gradients in each zone. These results are then visualized in Visit and the aforementioned phenomena are expected to be present.

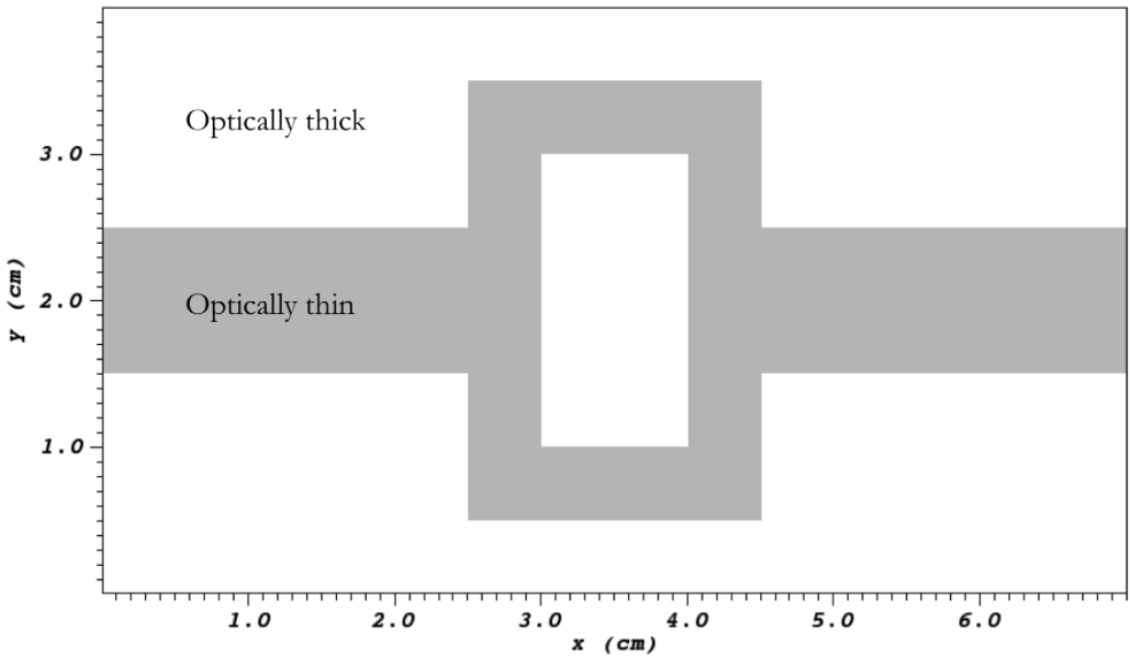

Figure 3.4: Schematic of the 2-D Tophat problem.

FINMCOOL's ability to set the random number seed allows for the same problem to be run with different seeds, which forms an ensemble mean and variance of the results. 20 simulations of the Tophat problem, with randomly selected seeds, were run with $\Delta x = \Delta y = 0.125$ cm and 100,000 particle histories per time step. The

ensemble mean of the results is equivalent to running a single problem with 2×10^7 particle histories, except with the added benefit of the standard deviation of the results.

3.3.1 Noise Reduction via Ensemble Averaging

Both gradient approximation methods are susceptible to stochastic noise from IMC, although reducing noise's effect is different for the two methods. The estimator is based on tallying particle histories, therefore increasing the number of particles in each time step is the key to reducing the variance of the estimator results. Finite difference is a linear approximation of the gradient, thus the spacing over which the linearization takes place is directly proportional to the error. As the grid spacing becomes smaller, the variance in the finite difference results is reduced. Further compounding the problem for the estimator, is that as the grid size becomes smaller, the total track length of particles in each zone is reduced, which exacerbates the noise problem for the estimator. A simulation with small grid spacing and a low number of particles would be the bane of the estimator. A simulation with these characteristics is compared against the ensemble average results for the finite difference method via a line out of the gradient magnitude at $x = 0.2$ cm and $y = 2.5$ cm in Fig. 3.5 and for the estimator in Fig. 3.6.

Figures 3.5 and 3.6 show that both methods are susceptible to noise, however the noise can be suppressed by performing an ensemble average and setting the simulation parameters correctly. Furthermore, they also show that the magnitude changed substantially between the two runs, which indicates the error in the 10^5 particle run may be quite high. It is likely, but difficult to prove, that the estimator results are more accurate than the finite difference results, since this behavior was observed in the 1-D absorber problem. The two methods should converge as the

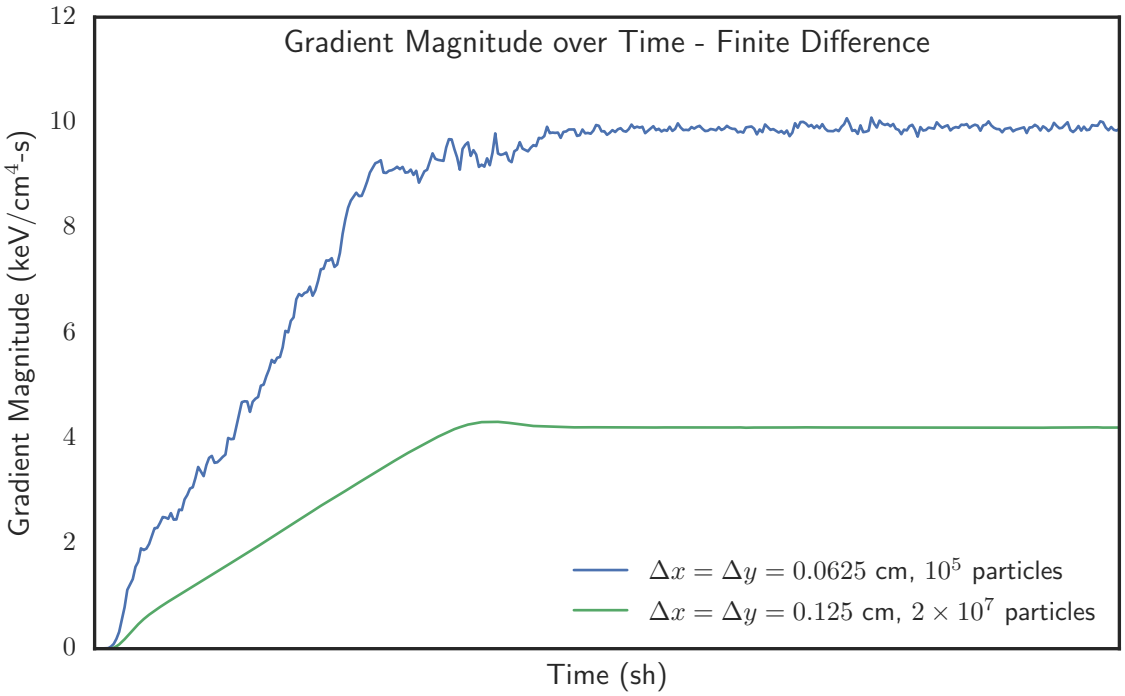

Figure 3.5: Net deposited energy density rate gradient magnitude, calculated with finite difference, over time.

number of particles is increased (for the estimator) and the grid is refined (for the finite difference method). However, it is computationally expensive to do so.

3.3.2 Ensemble Average Results

Figures 3.5 and 3.6 show that ensemble averaging can remedy the effects of stochastic noise on the net deposited energy density rate gradient. Figure 3.7 shows the magnitude of the gradient vector at $x = 0.2$ cm at various time steps. It illustrates that at early times the magnitudes are comparable between the simple finite difference (FD) and estimator (Est) methods, but that the results diverge over time.

Figure 3.7 shows that the magnitude of the vector is not consistent between the two methods. This confirms the results shown in Figs. 3.5 and 3.6. But, because an analytic solution is not available for this problem, it is unknown which method

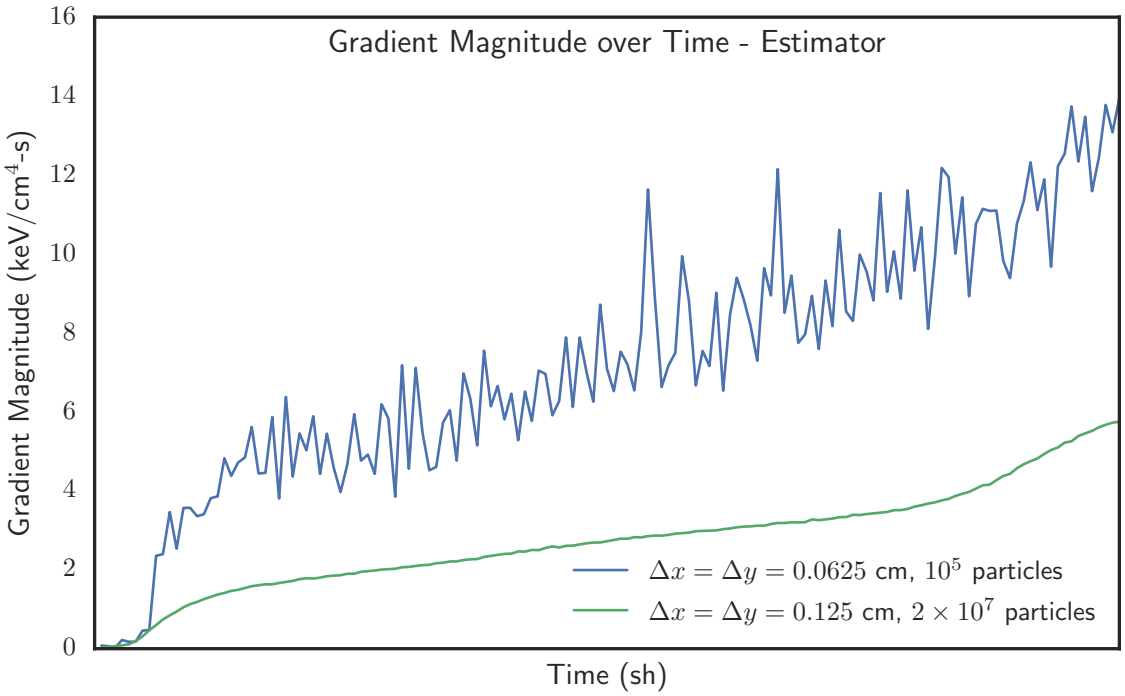

Figure 3.6: Net deposited energy density rate gradient magnitude, calculated with the estimator, over time.

is more accurate. However, this could be determined with enough computational resources. That being said, the direction of the gradient is equally important as the magnitude. Figure 3.8 shows the gradient vectors for the finite difference method (in reds) and the estimator (in greens) overlaid on the net deposited energy density rate at $t = 0.137476$ shakes.

From this is can be seen that the gradient direction is consistent between the two methods, and even the relative scaling between the methods is consistent (the size of the vector arrows are consistent between the methods) which implies there may be a systematic error in one of the two methods that is causing the magnitude difference between the two methods, since the relative magnitudes and directions are consistent between the finite difference and the estimator methods. With this data in hand, the

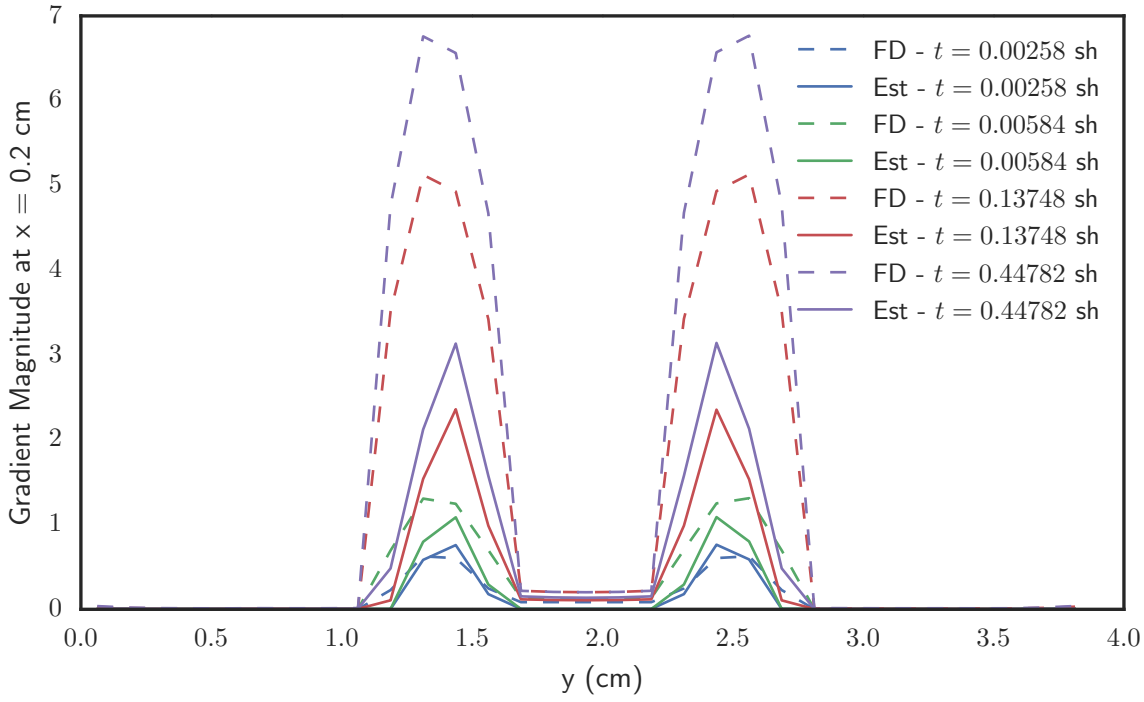

Figure 3.7: Net deposited energy density rate gradient magnitude approximations, estimator in solid and finite difference in dashed lines, at $x = 0.2$ cm at various time steps.

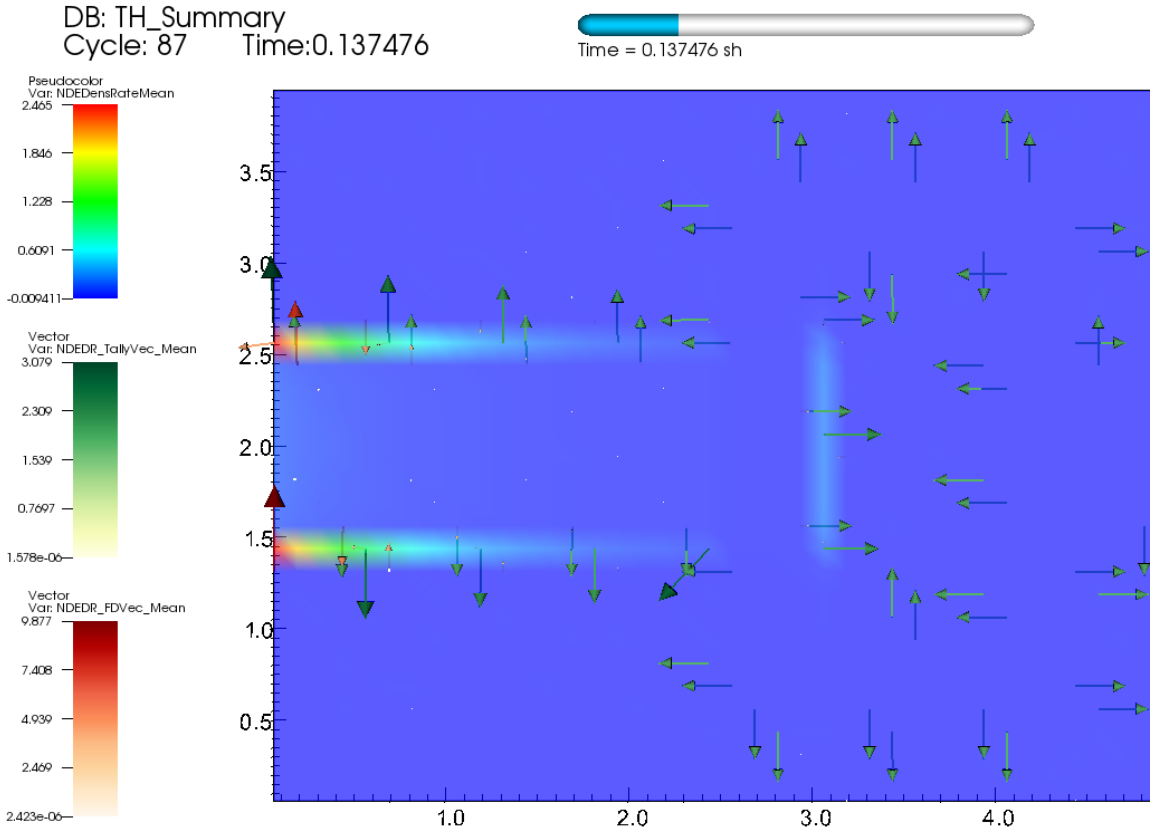

Figure 3.8: Net deposited energy density rate gradient approximations, estimator in greens and finite difference in reds, at $t = 0.137476$ shakes.

important question is, what is the benefit of the estimator over the finite difference method? The next section compares the variance of the two methods, which is the main driver of instability in the BHR-2 model.

3.3.3 Variance Comparison

With the ensemble average, the mean and standard deviation of the net deposited energy density rate Gradient in each zone was recorded for all 428 time steps. From this the relative standard deviation ($RSD = \sigma/\mu$) was calculated in each zone and then spatially-averaged for each time step. To understand if the estimator reduced the variability (or noise) in the gradient, compared to the finite difference method, the difference in the relative standard deviation was taken between the two methods: Estimator - Finite Difference. If the result is negative, the estimator reduced the variance. This is visualized in Fig. 3.9. The average difference, over all time steps, was a 312 % reduction. Thus, the estimator reduces the variance of the net deposited energy density rate gradient for a complex problem such as the Tophat. This is critical because of the direct coupling of the energy density to pressure gradient term in the BHR-2 model. Reducing the variance in the pressure gradient term was shown to directly increase the maximum stable time step. This decrease in computational cost is crucial to the ability to perform accurate and timely radiation-hydrodynamics simulations using IMC and BHR-2. The few large positive spikes are likely caused by time steps in which many spatial locations have a near zero or a large value. This can artificially skew the RSD difference, while the σ difference is not drastically different.

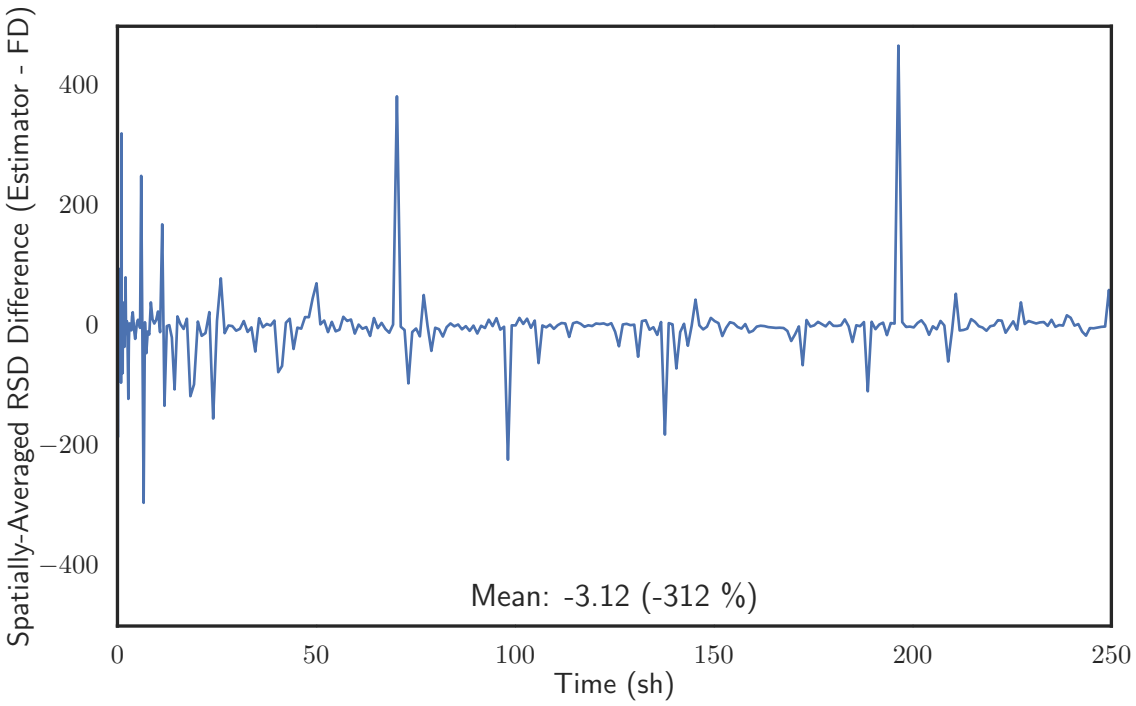

Figure 3.9: Difference in the spatially-averaged relative standard deviation over time: Estimator - Finite Difference. A negative value represents a reduction in the variance of the results. The average difference, over time, is -312 %.

4. CONCLUSIONS

In conclusion, the BHR-2 model was shown to have stability issues that stem from the pressure gradient term changing signs in relation to the mass-flux velocity. Reducing the variance in the pressure gradient term, reduced the possibility of this sign change, which in turn increased the maximum stable time step for the system. This increased time step size provides a decrease in the computational cost of radiation-hydrodynamics simulations using IMC and BHR-2.

To attempt to reduce the variance in the pressure gradient term, linear filters were applied to data from RAGE for a CH/Al shock tube problem. The filters were shown to be effective in reducing the variance, but they were an ad-hoc solution. The type of filter and number of times one should recursively apply the filters depended on the data, and simulation parameters. This type of ad-hoc, *a posteriori* solution is not a robust method for alleviating the scourge of IMC/BHR-2 noise.

Practical examples of RAGE simulations where BHR-2/IMC calculations crash, whereas other methods such as diffusion or no mix models do not crash, were presented. These problems were the impetus of the work presented herein. A finite element representation of the absorbed energy density was derived, because of the "tally-able" nature of Monte Carlo methods. This finite element estimator was implemented in FINMCOOL, an IMC code developed at Texas A&M, and run on a verification problem. The verification problem showed that the estimator was more accurate than finite difference methods, but at the expense of a slightly higher variance. It was expected that this increase in variance would decrease as the problem complexity increased. This assertion was verified after the results from a more complicated Tophat problem was investigated. The estimator was shown to be equally

affected by noise in low-fidelity problems, but after an ensemble averaging, the variance in the estimator results were 312% smaller than for the finite difference results. An analytic solution for the Tophat is not known, thus is was not possible to compare the accuracy of both methods, but because of the verification problem, it is expected that the estimator is also more accurate than the finite difference method.

4.1 Future Work

Future work should consist of generating a high-fidelity solution to the Tophat problem to estimate a convergence rate of both methods. Doing this would also allow one to compare the error in the ensemble average results for the estimator and finite difference results. This estimator may be implemented into radiation-hydrodynamics codes, such as RAGE, to decrease the computational cost associated with IMC/BHR-2 runs.

REFERENCES

[1] A. Banerjee, R. Gore, and M. Andrews. Development and validation of a turbulent-mix model for variable-density and compressible flows. *Physical Review E*, 82(4), Oct. 2010.

[2] D. Besnard, F. Harlow, R. Rauenzahn, and C. Zemach. Turbulence transport equations for variable-density turbulence and their relationship to two-field models. Technical Report LA-12303-MS, Los Alamos National Laboratory, Jun. 1992.

[3] N. Denissen, J. Fung, J. Reisner, and M. Andrews. Implementation and Validation of the BHR Turbulence Model in the FLAG Hydrocode. Technical Report LA-UR-12-24386, Los Alamos National Laboratory, Aug. 2012.

[4] J. Fleck and J. Cummings. An implicit Monte Carlo scheme for calculating time and frequency dependent nonlinear radiation transport. *Journal of Computational Physics*, 8(3):313–342, Dec. 1971.

[5] Sir W. Thomson F.R.S. XLVI. Hydrokinetic solutions and observations. *Philosophical Magazine Series 4*, 42(281):362–377, 1871.

[6] M. Gittings, R. Weaver, M. Clover, T. Betlach, N. Byrne, R. Coker, E. Dendy, R. Hueckstaedt, K. New, W. Oakes, D. Ranta, and R. Stefan. The RAGE radiation-hydrodynamic code. *Comput Sci Disc.*, 1(1):015005, oct 2008.

[7] Professor Helmholtz. XLIII. On discontinuous movements of fluids. *Philosophical Magazine Series 4*, 36(244):337–346, 1868.

[8] D. Israel, R. Gore, and K. Stalsberg-Zarling. Validating the BHR RANS model for variable density turbulence. In *39th AIAA Fluid Dynamics Conference.*

American Institute of Aeronautics and Astronautics (AIAA), Jun. 2009.

[9] M. Kalos and P. Whitlock. *Monte Carlo Methods*. Wiley, 2009.

[10] R. McClarren, T. Lane, and T. Urbatsch. The Scourge of IMC Noise on the BHR-2 Mix Model: A Study of the Issues with Nonlinear Coupled Physics. Technical Report LA-UR-15-20625, poster at JOWOG32M, Los Alamos National Laboratory, Feb. 2015.

[11] E. Meshkov. Instability of the interface of two gases accelerated by a shock wave. *Fluid Dynamics*, 4(5):101–104, 1969.

[12] Lord Rayleigh. Investigation of the character of the equilibrium of an incompressible heavy fluid of variable density. *Proceedings of the London Mathematical Society*, s1-14(1):170–177, Nov. 1883.

[13] R. Richtmyer. Taylor instability in shock acceleration of compressible fluids. *Communications on Pure and Applied Mathematics*, 13(2):297–319, May 1960.

[14] J. Schwarzkopf, D. Livescu, R. Gore, R. Rauenzahn, and J. Ristorcelli. Application of a second-moment closure model to mixing processes involving multicomponent miscible fluids. *Journal of Turbulence*, 12:N49, 2011.

[15] K. Stalsberg-Zarling and R. Gore. The BHR2 Turbulence Model: Incompressible Isotropic Decay, Rayleigh-Taylor, Kelvin-Helmholtz and Homogenous Variable Density Turbulence. Technical Report LA-UR-11-04773, Los Alamos National Laboratory, Aug. 2011.

[16] G. Taylor. The Instability of Liquid Surfaces when Accelerated in a Direction Perpendicular to their Planes. I. *Proceedings of the Royal Society of London A: Mathematical, Physical and Engineering Sciences*, 201(1065):192–196, 1950.

[17] A. Wollaber. *Advanced Monte Carlo Methods for Thermal Radiation Transport.* PhD thesis, University of Michigan, 2008.